Bone 209 (2026) 117914

Contents lists available at ScienceDirect

Bone

journal homepage: www.elsevier.com/locate/bone

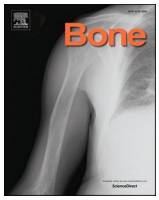

Full Length Article

PPy-coated wire actuators for micromechanostimulation of cells – identification of immediate-early responsive mechanoregulatory genes in osteoblasts

Jiamin Chen [a], Amaia B. Ortega-Santos [b], Satoru Hayano [c], Ziyi Wang [d], Jose G. Martinez [b], Emilio Satoshi Hara [e], Edwin W.H. Jager [b], Hiroshi Kamioka [a,*]

[a] Department of Orthodontics, Okayama University Graduate School of Medicine, Dentistry and Pharmaceutical Sciences, Okayama, Japan
[b] Department of Physics, Chemistry and Biology (IFM), Linköping University, Linköping, Sweden
[c] Department of Orthodontics, Okayama University Hospital, Okayama, 700-8525, Japan
[d] Department of Molecular Biology and Biochemistry, Okayama University Graduate School of Medicine, Dentistry and Pharmaceutical Sciences, Okayama, 700-8525, Japan
[e] Department of Advanced International and Information Dentistry, Okayama University Graduate School of Medicine, Dentistry and Pharmaceutical Sciences, Okayama, Japan

ARTICLE INFO

Keywords:
Mechanotransduction
Mechanostimulation
Osteoblasts
Polypyrrole

ABSTRACT

Mechanotransduction, i.e., the conversion of mechanical cues into biochemical signals, is essential for bone development, remodeling, and adaptation. Although mechanical loading is known to regulate osteoblast function and bone homeostasis, dissecting the early and sustained mechanotransductive responses at the microscale remains challenging due to limitations of existing in vitro models. Here, we report the development and application of a mechanostimulation system comprising a polypyrrole (PPy)-based wire actuator that expands and contracts (4 μm in radius) upon electrical actuation and enables precise, localized micromechanical stimulation of a small number of cells within standard culture formats. Using this system, we applied short-term (30 min) cyclic (Cyc30) or static (Stat30), as well as prolonged (120 min) cyclic (Cyc120) stimulations to two osteoblast-like cells (MC3T3-E1 or KUSA-A1). Subsequent transcriptomic profiling and computational network analyses revealed that Cyc30 was not capable of inducing significant changes in mRNA expression, suggesting cellular adaptation to short-term cyclic loading. In contrast, Stat30 induced the upregulation of *Fos*, *Btg2*, *Egr1*, and *Fosl1*, all known genes associated with mechanotransduction, supporting the validity and reproducibility of our experimental mechanostimulation system. Notably, two long non-coding RNAs (B930036N10Rik and 5430431A17Rik) were identified for the first time as being upregulated in response to Stat30 stimuli. Among the differentially expressed genes (DEGs) upregulated by Cyc120 stimuli, *Hmox1*, a stress-inducible enzyme known for its roles in maintaining cellular homeostasis and promoting survival, was the only DEG repeatedly observed across the Cyc30/Cyc120 and Stat30/Cyc120 comparisons in both cell types, potentially emerging as a key stress-response gene under prolonged mechanical loading. Collectively, these results establish the PPy-based microactuator as a powerful tool for microscale mechanobiology, and provide molecular insight into immediate-early responsive transcriptional programs underlying osteoblastic mechanoadaptation conserved across different cell types.

1. Introduction

Mechanotransduction—the process by which cells convert mechanical stimuli into biochemical signals—is a fundamental mechanism that underpins a wide array of physiological and pathological processes. [1,2] It plays a critical role in tissue development, homeostasis, healing, ageing, as well as in diverse pathological scenarios such as in the progression of diseases, including osteoporosis, fibrosis, and cancer. [3,4]

Bone-loss-related disorders, such as osteoporosis, significantly increase the risk of fractures, chronic pain, and long-term disability, collectively affecting more than 200 million individuals worldwide and placing a growing burden on healthcare systems. [5] In addition, as life

* Corresponding author.
E-mail address: kamioka@md.okayama-u.ac.jp (H. Kamioka).

https://doi.org/10.1016/j.bone.2026.117914
Received 9 February 2026; Received in revised form 29 April 2026; Accepted 29 April 2026
Available online 30 April 2026

expectancy continues to rise and the global population ages, there is an increasing need for more effective strategies to support bone maintenance and promote regeneration beyond conventional pharmacological and surgical approaches. In particular, emerging strategies targeting bone mechanoregulation are becoming increasingly important for managing bone-related diseases and improving long-term quality of life.

It has been well-established that mechanical loading can inhibit bone resorption and increase bone formation in vivo. [6,7] This process, known as bone remodeling, adjusts bone shape and structure to meet various mechanical demands through coordinated cellular activities that regulate bone resorption and formation across cortical and cancellous surfaces. [6] These remodeling events result in a modeling drift, where structural units of bone are repositioned over time in directions influenced by growth patterns, allowing the skeleton to optimize mass distribution according to mechanical stress. [8,9] Mechanical stimuli also play key roles in regulating osteoblast function on the bone surface, directing their differentiation into osteocytes. [10]

Recent advances in molecular and cell biology have uncovered that mechanical signals are actively shaping cellular behavior through intricate signaling networks involving integrins, cytoskeletal tension, ion channels, and nuclear mechanosensors. [11] Mechanical forces can modulate the organization of the cytoskeleton and influence nuclear architecture ("tensegrity"), leading to transcriptional changes that drive the function and fate of cells. [12,13] To further obtain deeper insight into the molecular mechanisms related to mechanostransduction, several in vitro models with strictly controlled experimental conditions have been developed. [11,14] At the macro-scale, mechanical stimuli were applied to the entire bone tissue, including human bones, by using a universal testing machine. [15–17] Although these models allow the analysis of the entire tissue, they typically involve more complex experimental settings and timeframes ranging from several hours to weeks. Consequently, this scale of testing makes it challenging to resolve the rapid signaling events and intercellular interactions that occur at the cellular level shortly after stimulation. [15]

At the sub-tissue level, a stepping motor has been used to apply mechanical stimuli to the entire cell population cultured on stretchable substrates (e.g., PDMS). [18] More recent technologies employ microfabricated platforms and 3D culture systems to recapitulate tissue-specific mechanical environments with improved spatial and temporal resolution. [19–21] However, these approaches often face limitations in precisely mimicking the dynamic, localized, and multiaxial mechanical stimuli that cells encounter in vivo. Moreover, many of these systems do not enable the application of microscale forces directly to specific regions of the cell culture or to modulate force magnitude and frequency in real time.

At a sub-cellular scale, techniques such as atomic force microscopy (AFM) offer high-resolution measurements of cell stiffness and force response, with precise control over localized mechanical stimuli. [22–24] These methods are highly quantitative and allow investigation of individual molecular interactions at the sub-micron level. However, these nanoscale analyses are limited to a narrow area for physico-structural analyses of, for instance, collagen fibers and individual cells, making it difficult to access cell-cell interactions and mechano-transduction signaling. [22,25]

To overcome these limitations, we have developed a new electrically expandable microactuator that enables direct mechanical stimulation of a few cells. The micromechanical stimulation system was designed to be placed inside standard culture plates and generate/deliver localized micromechanical stimulations to cells through radial expansion of a polypyrrole/gold (PPyAu) wire actuator. [26] This PPyAu wire actuator can be controlled to induce cyclic or static mechanical stimulations to adjacent cells, mimicking both the dynamic and static microstrains experienced by osteoblasts. [27] Accordingly, the objective of this study was to employ this system to apply short-term (30 min) and prolonged (120 min) stimulations under cyclic or static loading regimes, and by coupling it with transcriptomic analyses, we aimed to identify and compare immediate-early mechanosensitive gene networks and biological processes conserved across two different osteoblast-like cell types: MC3T3-E1 pre-osteoblasts and KUSA-A1 mesenchymal stromal cells.

2. Materials and methods

2.1. Fabrication and characterization of PPyAu wire actuators

The PPyAu wire actuators were produced as described (*Ortega-Santos* et al*, Small Science under revision*). Shortly, a 20 μm layer of polypyrrole was electrochemically deposited at 0.3 mA/cm (per centimeter of wire immersed in the electropolymerisation solution) on the 500 μm diameter Au wires (GoodFellow Inc.) from a 0.1 M Pyrrole (Sigma Aldrich), 0.1 M NaDBS (Sigma Aldrich) aqueous solution. Next, the PPyAu wires were pre-actuated upon 10 square wave potentials stepping between −0.7 V and 0.3 V, for 150 s at each potential limit, in 0.1 M NaDBS aqueous solution and left in the same oxidized (contracted) state.

To measure the expansion of the needle in real time, we used a laser scanning micrometer (LSM). The system comprises a beam emitter and beam detector unit (Mitutoyo LSM-501H) and a controller (Mitutoyo LSM-6100). The emitter produces a highly collimated red laser beam (640 nm) that is scanned horizontally across the measurement region and detected on the opposite side. When the wire actuator is placed between the emitter and detector, a portion of the laser beam is obstructed, producing a shadow on the detector that corresponds to the wire diameter. Continuous monitoring of changes in this shadow enables real-time measurement of diameter variations of the wire. The LSM controller converts the measured diameter into a voltage output signal, which is transmitted to a computer and synchronized with electrochemical data acquired from the potentiostat (Autolab PGSTAT204). From the diameter measurements using the LSM, the thickness of the electropolymerized PPy ($\delta poly$), the polymer expansion ($\measuredangle\delta$) during actuation (expansion/contraction), and the radial actuation strain of the PPyAu wire were calculated using the following equations:

$$Polymerisation\ thickness\ (\mu m) : \delta_{poly} = \frac{D_{polymer} - D_{bare\ wire}}{2} \quad (1)$$

$$Polymer\ expansion\ (\mu m) : \Delta\delta = \frac{D_{expanded} - D_{contracted}}{2} \quad (2)$$

$$Strain\ (\%) = \frac{\Delta\delta}{\delta_{poly}}$$

where D refers to the diameter. [27]

2.2. Cell culture

Two osteogenic cell lines, MC3T3-E1 (mouse pre-osteoblasts) and KUSA (mouse mesenchymal stem cells), were used in this study. Cells were maintained in complete culture medium: Minimum Essential Medium Alpha (α-MEM; Cat# 135–15,175, FUJIFILM Wako Pure Chemical Corporation, Osaka, Japan) containing L-glutamine and phenol red, supplemented with 10% fetal bovine serum (FBS; Cat# 175012, NICHIREI BIOSCIENCES INC., Tokyo, Japan) and 1% penicillin-streptomycin (P/S; Cat# 15140–122, Gibco, Grand Island, NY, USA). Cultures were incubated at 37 °C in a humidified atmosphere containing 5% CO_2.

For each experiment, 1.5×10^5 cells were seeded per insert and cultured for 24 h. Cells were cultured in a collagen membrane culture insert (AteloCell Atelocollagen, CM-24, KOKEN Co., Ltd., Tokyo, Japan) designed for 24-well plates (Costar, Cat# 3738, Corning Inc., Grand Island, NY, USA). Each insert featured a soft, membrane-like bottom, providing a compliant substrate that mimics the mechanical properties of the native extracellular matrix. For each culture, 500 μL of cell suspension was added inside the insert, and an additional 500 μL of

complete culture medium was added outside the insert to maintain hydration and allow nutrient diffusion across the membrane. The effective culture area of each membrane was 64 mm^2. After reaching confluence, the PPyAu wire actuator was carefully penetrated through the central region of each culture insert.

2.3. Micromechanical stimulation

Micromechanical stimulation of the cultured cells was performed using the customized three-electrode electrochemical configuration adapted for use in a 24-well culture plate. A thin, pliable stainless-steel woven sheet (Easipet), which was used as the counter electrode, was arranged to line the inner walls of each well, with a small extension left protruding beyond the plate edge to permit attachment to the electrical connectors. Two holes, each 1 mm in diameter, in the plate lid to allow the PPyAu wire actuator and an Ag wire (pseudo-reference electrode) to be inserted vertically at the center and at the periphery of the well, respectively. To eliminate mechanical artefacts caused by cable movement, the PPyAu wire actuators were immobilized using laboratory silicone (Shofu, Kyoto, Japan). Thin external cables connected the three-electrode system to the potentiostat (Autolab PGSTAT204, Metrohm, Herisau, Switzerland), enabling all electrical operations to be performed without opening the incubator door. The PPyAu wire actuators were sterilized by immersion in 70% ethanol for 30 s and rinsed afterwards with MEM culture medium before insertion into the well. Before the application of mechanical stimuli, the cells were seeded onto the collagen-coated membrane and allowed to adhere for 24 h prior to the insertion of the PPyAu wire actuator. The actuator was then forcedly inserted vertically through the center of the pre-established cell layer and underlying collagen membrane. Once the system was assembled, the cells were left to stabilize for an additional 12 h to enable cellular adaptation and the establishment of direct, tight physical contact between the cells and the actuator surface. [27] This ensured efficient mechanical coupling, such that radial expansion of the PPy layer (~4 μm) was directly transmitted to the surrounding cell–matrix environment. Representative images and videos of the mechanical stimulation using the same PPyAu wire actuator have been reported previously. [27]

The stimulation of the cells was performed by applying 18 (cyclic stimulation for 30 min, Cyc30) or 72 cycles (cyclic stimulation for 120 min, Cyc120) of square wave potentials stimuli ranging from −0.7 V to +0.3 V, with 100 s at each potential limit, or by a single potential pulse (static stimulation of 30 min, Stat30) at −0.7 V. A potentiostat (Metrohm AutoLab PGSTAT204) controlled by Nova 2.1 software was used to operate the electrochemical cell and record the electrochemical data. As controls, 2 different experiments were designed. For *Control 1* (Cont1-NS), a PPyAu wire actuator was inserted through the cell-seeded membrane without applying any current. For *Control 2* (Cont2-NC), a bare Au wire was also inserted through the cell membrane and the same stimulation protocols were applied.

2.4. Finite element model (FEM)

A two-dimensional (2D) FEM was developed to estimate the spatial distribution of actuator-induced deformation and strain. The membrane was modeled as a linear, isotropic elastic solid under plane-stress conditions. This simplification was adopted to represent the thin composite structure consisting of a collagen membrane (thickness: 2.4 ± 0.2 μm; [28] Young's modulus: 0.54 ± 0.23 MPa [29]) and an adherent osteoblast layer (thickness: 5 μm; [30,31] Young's modulus: 5 kPa [32]). Assuming perfect bonding between the collagen and cell layers, an effective composite modulus was calculated using a thickness-weighted rule of mixtures:

$$Eeff = \frac{(Ec \cdot tc) + (Eo \cdot to)}{tc + to}$$

where *Ec* and *tc* denote respectively the Young's modulus and thickness of collagen, and *Eo* and *to*, those of the osteoblast layer. This yielded an approximate modulus of ~178.51 kPa. The composite membrane was assumed to exhibit a near-incompressible material behavior, with an effective Poisson's ratio = 0.499. [33] The inner boundary of the computational domain was defined by the 270 μm radius of the PPy-coated actuator (comprising a 500 μm diameter gold wire with a 20 μm PPy coating). [27] The outer radius was derived from the manufacturer-specified culture area of 64 mm^2, corresponding to an equivalent circular radius of 4513 μm.

The domain was discretized using triangular finite elements (~50,000 elements and 25,000 nodes), with adaptive mesh refinement applied near the inner boundary to accurately resolve steep displacement and strain gradients. Mechanical loading was imposed as a prescribed radial displacement of 4 μm at the inner boundary, corresponding to the experimentally measured expansion of the PPyAu wire actuator, while the outer boundary displacement was fixed (u=0). The governing equations of linear elasticity were solved under plane-stress conditions using a Python-based finite element framework (scikit-fem).

Radial displacement (ur) was extracted and used to compute strain components in cylindrical coordinates: circumferential strain: $\varepsilon\theta = ur / r$ and radial strain: $\varepsilon r = dur / dr$. To capture the full in-plane mechanical state, principal strains were calculated as maximum principal strain (ε_max) and minimum principal strain (ε_min), which correspond, under axisymmetric conditions, approximately to circumferential and radial strain, respectively.

Postprocessing was performed by extracting radially averaged displacement profiles from the FEM solution. From these, strain components were derived as follows: circumferential strain (εθ) was estimated as $\varepsilon\theta = ur/r$, and radial strain (εr) was computed as the spatial derivative $\varepsilon r = \partial ur/\partial r$. The maximum principal strain (ε_max) and minimum principal strain (ε_min) were approximated by the circumferential and radial strain components, respectively, consistent with the axisymmetric deformation of the system. To reduce numerical oscillations arising from spatial differentiation, the radial strain profile (and corresponding minimum principal strain) was lightly smoothed for visualization purposes using a local polynomial filter, without altering the underlying FEM displacement field or quantitative analyses. All reported numerical values were obtained from the unsmoothed data unless otherwise stated. Radial binning was used to obtain smooth spatial profiles without artificial interpolation.

Circumferential stress (σθ) was approximated using Hooke's law ($\sigma\theta = E \cdot \varepsilon\theta$).Mechanical metrics were further integrated over a circular region of 5 mm diameter (radius 2500 μm), corresponding to the biopsy punch used for RNA extraction.

To assess the validity and possible generalizability of this model, a sensitivity analysis was performed by varying across experimentally plausible ranges, the collagen thickness (2–10 μm), collagen modulus (0.3–10 MPa), cell-layer thickness (5–20 μm), and cell-layer modulus (4–10 kPa). For each parameter combination, the effective composite modulus was recalculated and the FEM solution recomputed. Displacement, circumferential strain, radial strain and principal strain values were extracted at defined radial distances (1000 μm and 2500 μm) and normalized to the analytical interface strain (~14,800 με).

2.5. RNA sequencing

Total RNA was extracted using the RNeasy Mini Kit (Qiagen, Hilden, Germany) according to the manufacturer's protocol, immediately after the completion of the mechanostimulation protocol to capture the immediate-early transcriptional landscape before mRNA degradation or secondary signaling cascades occurred. To isolate RNA from specific regions of the culture insert, particularly from cells located adjacent to the PPyAu wire actuator, cells were harvested using a 5 mm diameter biopsy punch (KAI Industries Co., Ltd., Gifu, Japan; effective sampling

area ~ 20 mm^2). This targeted collection approach enabled region-specific gene expression analysis by collecting cells from approximately one-third of the total membrane area (64 mm^2), thereby facilitating precise profiling of mechanosensitive responses.

Extracted RNA samples were submitted to Azenta Life Sciences (South Plainfield, NJ, USA) for RNA sequencing (RNA-seq) analysis. Library preparation, high-throughput sequencing, and primary bioinformatics processing were performed by the service provider following standardized protocols.

After quality trimming with Trim Galore v0.6.10, the reads were aligned to the GRCm38.108 reference genome (Ensembl Release 113) using the STAR aligner v2.7.10b. De novo transcript assembly and annotation were performed using StringTie v2.2.1 and SQANTI3 v5.0. Transcript-level quantification was performed for all samples using Salmon v1.9.0, followed by further quality filtering with isoformSwitchAnalyzeR v1.17.05, based on Salmon's mapping results.

2.6. Differential gene expression analysis

Differentially expressed genes (DEGs) were identified separately for MC3T3-E1 and KUSA-A1 cells across all experimental comparisons. RNA-seq raw counts were first normalized and analyzed using DESeq2 (v1.31.16) in R (v4.3.2). Genes were considered significantly differentially expressed when meeting both of the following criteria: $|\log_2 \text{fold change}| \geq 1.0$, and adjusted P value (FDR) < 0.05 (Benjamini–Hochberg correction). FastQ files have been uploaded in the Gene Expression Omnibus (GEO) database under the accession number GSE314317.

Each mechanical stimulation condition (Cyc30, Stat30, and Cyc120) was compared with its corresponding control (Cont1-NS or Cont2-UC), and additional pairwise comparisons were performed between stimulation regimens (Cyc30 vs Stat30, Cyc30 vs Cyc120, and Stat30 vs Cyc120). For each comparison, DEGs were classified as upregulated or downregulated, and the number of DEGs per category was tabulated for each cell type.

To identify transcriptional responses conserved across cell types, DEGs from MC3T3-E1 and KUSA-A1 were compared for each condition. Gene lists from both cell types were intersected to determine common DEGs meeting significance thresholds in both cell lines. These intersecting genes were then categorized into upregulated or downregulated groups according to their direction of change in both datasets.

Instead of plotting circular Venn diagrams, results were visualized in a tabular Venn-style matrix, summarizing: the total number of DEGs in each cell type for each comparison, the number of shared (common) DEGs across both cell types, and detailed gene lists including gene names, encoded proteins, and functional annotations.

For gene annotation, the protein names and biological annotations for all DEGs were retrieved from the publicly available database UniProtKB. Annotations were manually curated and simplified to show concise descriptions of gene functions.

2.7. Gene ontology biological process (GO-BP) enrichment analysis

Initial GO-BP enrichment analysis was performed separately for MC3T3-E1 and KUSA-A1 cells, for each pairwise comparison of mechanical stimulation conditions (Cyc30 vs Cont1-NS, Cyc30 vs Cont2-UC, Stat30 vs Cont1-NS, Stat30 vs Cont2-UC, Cyc120 vs Cont1-NS, Cyc120 vs Cont2-UC, Cyc30 vs Stat30, Cyc30 vs Cyc120, and Stat30 vs Cyc120) by using clusterProfiler v4.6.0. Lists of significantly upregulated and downregulated DEGs ($|\log_2 FC| \geq 1.0$; FDR < 0.05) were used as input. Significance threshold: adjusted P value (FDR) < 0.05. Enriched GO-BPs were classified as either upregulated or downregulated, corresponding to the directionality of the DEGs driving each term.

To identify biological processes consistently regulated across both cell types, enriched GO-BPs in each cell were compared for each stimulation condition and the results were organized into Venn-style tables summarizing the total number of enriched GO-BPs detected in each cell type, the number of intersected/shared GO-BPs observed in both cells, and directionality (upregulated or downregulated) for each comparison.

GO-BP networks were generated using ClusterProfiler (cnetplot) and enrichplot, which map DEGs to their associated enriched GO-BPs. In each network panel, Nodes represent individual GO-BPs or genes. Node color corresponds to adjusted P value ($-\log_{10}$FDR). Node size reflects gene set size or significant contribution. Edges represent gene-to-GO term relationships, allowing visualization of clustering and functional connectivity among enriched pathways. GO networks were exported as high-resolution vector graphics and color-coded by comparison to facilitate interpretation of biological processes activated under each mechanical stimulation regime.

2.8. Gene–gene interaction networks

All DEGs identified across the mechanical stimulation conditions and common to both MC3T3-E1 and KUSA-A1 cells were used to construct gene–gene interaction networks. We used the R package "CBNplot" to construct a Bayesian inferred gene regulatory network for the interaction inferences. The full set of DEGs (no prefiltering by pathway or annotation) served as input to allow unbiased identification of gene regulatory relationships.

For each gene pair, interaction strength was calculated using random forest–based feature importance measures, and directional edges were estimated by Bayesian network inference. For edges with available ChIP-seq evidence (via ENCODE and ChEA databases), interactions were rendered as solid lines. Edges inferred solely from Bayesian inference without direct binding evidence were plotted as dashed lines. Edge color represents correlation direction (red = positive, blue = negative), and edge width corresponds to interaction strength. Nodes represent individual DEGs, with node size proportional to normalized expression ($\log_2$TPM), and node color indicating gene function (e.g., transcription factor, stress response gene, uncharacterized gene). Circular ring plots around nodes represent the relative contributions of each gene to outgoing or incoming interactions.

Because YAP/TAZ-mediated signaling is a well-established and canonical mechanotransduction pathway, an additional mechanotransduction-specific interaction analysis was performed by incorporating Yap1 and Wwtr1 (Taz) as anchor nodes. These genes were forcibly included in the GRN inference to evaluate whether DEGs interact upstream or downstream of these mechanoresponsive transcriptional co-activators.

To accomplish this, Yap1 and Wwtr1 were added to the DEG list and reanalyzed with the same inference pipeline. Directional and correlational edges were recalculated, and the resulting mechanotransduction-centered networks highlight potential regulatory relationships among DEGs mediated via YAP/TAZ pathways. Interactions involving Yap1/Wwtr1 were visualized with thickened arrows (teal), and outgoing edges from YAP/TAZ were distinguished to show putative mechanotransduction-driven transcriptional cascades.

All interaction networks were visualized using Cytoscape v3.10 with custom graphical parameters. Node colors: grouped by functional category (stress response, transcription factor, ECM-related, apoptosis-related, unknown). Ring plots: multi-color rings indicating interaction direction-specific contribution. Arrowheads: direction of predicted regulatory influence. Dotted vs. solid edges: Bayesian-only inference vs. Bayesian + ChIP-seq validated interactions. Red–blue color scale: correlation coefficients (positive to negative).

2.9. Literature mining and topic association analysis

A literature mining analysis [34,35] of the PubMed database identified genes correlating with PubMed query results. A variable R was used to assess the correlation between the gene list and PubMed queries, calculating the ratio of query-and-gene-related articles to gene-related

articles. The co-occurrence probability of each gene with PubMed query in at least K articles was statistically analyzed, applying a *P*-value formula:

$$P = 1 - \sum_{i=0}^{k-1} f(i) = 1 - \sum_{i=0}^{k-1} \frac{\binom{k}{i}\binom{N-K}{n-i}}{\binom{N}{n}} \quad (3)$$

where N represents the total number of articles in PubMed, K is the number of articles related to the PubMed query, n, and k indicate the numbers of articles for a specific gene and those corresponding to the PubMed query, respectively. The nominal *p*-value was adjusted to FDR using the Benjamini-Hochberg approach. Genes with R values above $10K/N$ and FDR or *P*-value (if $K < 100$) lower than 0.05 were considered significant.

We performed this literature-based association analysis across several predefined biological themes: "Osteoblast", "Mechanotransduction", "Stress", "Apoptosis", and "Autophagy" with all DEGs identified across the mechanical stimulation conditions and common to both MC3T3-E1 and KUSA-A1 cells.

For each DEG, PubMed titles and abstracts were queried using the following search syntax: "Gene Symbol" AND "Mechanotransduction, Cellular"[Mesh], "Gene Symbol" AND "Osteoblasts"[Mesh], "Gene Symbol" AND Stress, Mechanical"[Mesh], "Gene Symbol" AND "Apoptosis"[Mesh], "Gene Symbol" AND "Autophagy"[Mesh], and their combined terms, e.g., "Gene Symbol" AND ("Osteoblasts"[Mesh] AND "Stress, Mechanical"[Mesh]), and "Gene Symbol" AND ("Osteoblasts"[Mesh] AND "Mechanotransduction, Cellular"[Mesh]).

Two quantitative metrics were calculated to place each gene in a two-dimensional association space: Topic relevance score (x-axis: $\log_2[1/P\text{-value}]$). *P*-values were computed from a hypergeometric distribution comparing the number of publications linking a gene to a topic versus the total publication background for that gene. Higher values indicate stronger topic-specific enrichment. Higher values indicate more topic-specific associations. Bubble size corresponds to the total number of topic-linked publications for each gene, while bubble color represents the $\log_{10}$ of all gene-related articles (proxy for gene popularity). Details of the setup environment, functions and queries can be found in the following website: http://ppybcell.bs-gou.com.

3. Results and discussion

3.1. Characterization and performance of the PPyAu wire actuator

The details of the fabrication and verification of the PPyAu wire actuator are presented elsewhere. [27] In brief, upon application of electrical potential, the electroactive PPy (electropolymerized in the presence of dodecylbenzenesulfonate, DBS) layer (approximately 20 μm thick) on the 500 μm Au wire undergoes reversible volumetric expansion and contraction, generating radial mechanical displacements (Fig. 1A). [26,36,37] The radial expansion of the PPyAu wire actuator was approximately 4 μm, as measured using a laser scanner micrometer

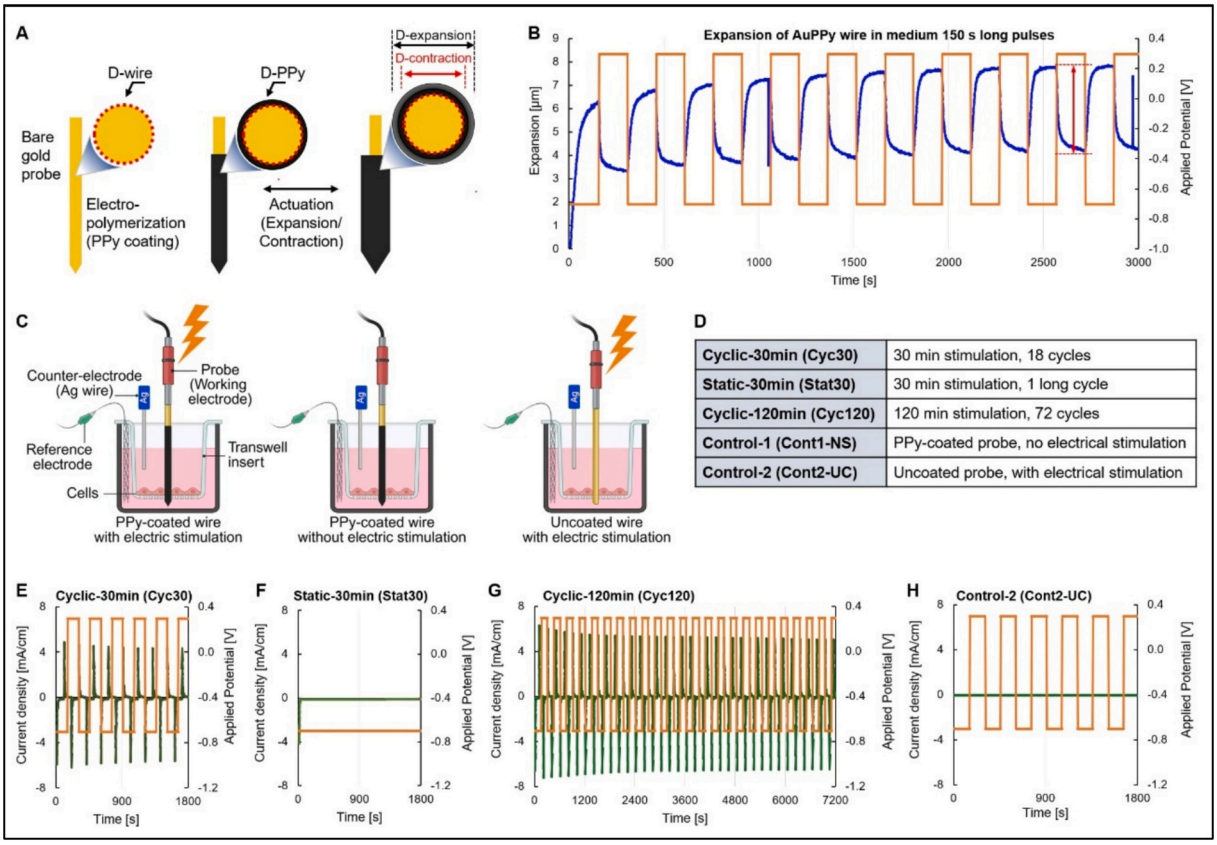

Fig. 1. Characterization of PPyAu wire actuator, experimental design, and current analysis. (A) Schematic representation of the PPyAu wire actuator fabrication and actuation. (B) Radial actuation of the PPyAu wire upon cyclic stimulation, with each potential held at −0.7 V and 0.3 V for 150 s, measured with a non-contact optical laser scanner. (C) Schematic representation of the mechanical and/or electrical stimulation setup applied to cells cultured in atelocollagen permeable membrane culture (transwell) inserts. (D) Summary of five experimental conditions: I- Cyclic-30 min (Cyc30): 30-min cyclic stimulation (18 cycles); II- Static-30 min (Stat30): 30-min static stimulation (1 cycle); III- Cyclic-120 min (Cyc120): 120-min cyclic stimulation (72 cycles); IV- Control1-nonstimulated (Cont1-NS): PPyAu wire actuator without electricity; V- Control2-Uncoated (Cont2-UC): bare Au wire with electrical stimulation. (*E*-H) Representative current vs. time (potential applied to the actuator). Orange square wave: Input voltage. Green line: Current response. For Cont1-NS, no electricity was applied, thus no plot is shown. (For interpretation of the references to color in this figure legend, the reader is referred to the web version of this article.)

(Fig. 1B). For subsequent mechanical stimulations, a frequency of 0.01 Hz, which is lower than typical physiological oscillations (e.g., 1 Hz), was chosen to optimize the expansion of the PPy layer. The electrochemical response of the PPy layer in cell culture medium is rate-limited by ion diffusion, requiring sufficient time to achieve maximum volumetric expansion (Fig. 1B). In this system, higher frequencies could also be applied but would result in attenuated radial displacement due to these inherent diffusion limits, as can be deducted from Fig. 1B. A detailed analysis on the effect of PPy thickness and actuation period (frequency) on the achieved maximum expansion has been reported previously [27].

As illustrated schematically in Fig. 1C, the radial actuation (Δδ) transmitted local compressive forces directly to cells, previously cultured on atelocollagen permeable membrane culture inserts. The stimulation of the cells was performed according to the conditions shown in Fig. 1D, by applying cycles of square wave potential stimuli stepping between −0.7 V and + 0.3 V, with 100 s at each potential limit. The consumed charge by the working electrode vs. time is shown in Suppl. Fig. 1.

Under short-term (Cyc30: 18 cyclic pulses over 30 min) or prolonged (Cyc120: 72 cyclic pulses over 120 min) cyclic stimulation, steady square-wave potentials were applied (Fig. 1E and G, orange traces) and current responses were measured (green traces). The consumed charge by the working electrode vs. time in each condition is shown in Suppl. Fig. 2. The stable response pattern indicated high electrical stability of the PPyAu wire actuator, maintaining uniform actuation without signal drift. This repeated on–off modulation resulted in continuous loading and unloading of osteoblast membranes. While the frequency and magnitude are lower than macro physiological strain (e.g., during locomotion), our system allows for the investigations of cellular responses to discrete, localized micromechanical deformations.

In contrast, the short-term static stimulation (Stat30: single pulse over 30 min) consisted of a single electrical stimulation at the start of the experiment, inducing a single expansion of the PPyAu wire actuator without subsequent contraction. This resulted in a sustained static mechanical load on the surrounding cells throughout the 30-min stimulation period (Fig. 1F), characterized in the electrochemical signal by a current peak at the beginning with negligible current flow thereafter.

The control experiments provided crucial insights into the specificity of the observed mechanical effects. Control-1 (non-stimulated: Cont1-NS) employed the same PPyAu wire actuator but without electrical stimulation, demonstrating that the polypyrrole coating alone did not trigger measurable bioresponse or other interference with cells. Control-2 (uncoated: Cont2-UC) used an uncoated Au wire with the same electrical stimulation to investigate the effect of the applied current on the cells (i.e., without mechanical stimulation) (Fig. 1H).

The combination of these conditions was used to validate the system as a reliable biomechanical platform for studying mechanosensitive responses of bone-forming cells under well-defined stimulation parameters. Representative images of cells attached to the PPyAu wire actuator surface and their displacement following actuation are provided in Fig. 2.

To explore how the applied mechanical strain could be transmitted to cells within this system, we performed 2D FEM of the actuator-induced deformation using a near-incompressible material model (Poisson's ratio $\nu = 0.499$) to better approximate the mechanical

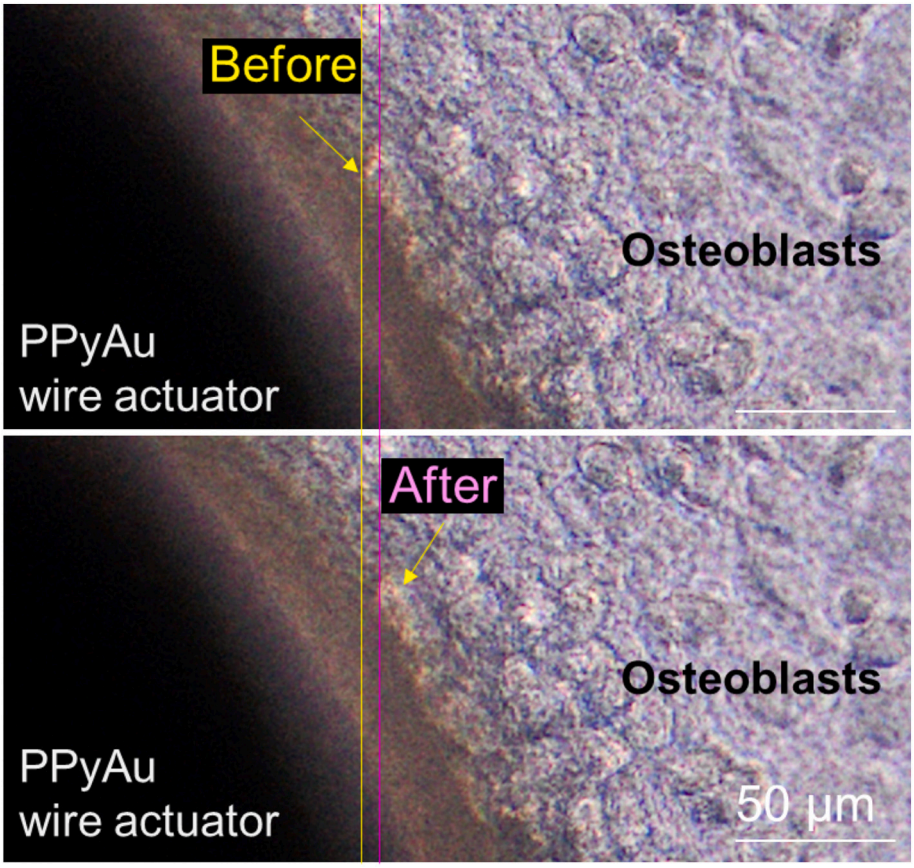

Fig. 2. Brightfield images showing osteoblasts in direct contact with the PPyAu wire actuator before (top) and after (bottom) mechanostimulation. The PPyAu wire is visible on the left, with the osteoblast cell layer on the right. Following actuation, radial expansion of the PPy coating (~4 µm) results in a measurable outward displacement of the surrounding cells, leading to local compression and deformation of adjacent osteoblasts. Yellow line indicates the position of a specific osteoblast (yellow arrow) before actuation. Pink line indicates the position of the same cell after actuation. The distance between the yellow and pink lines is ~4 µm. Scale bar: 50 µm. (For interpretation of the references to color in this figure legend, the reader is referred to the web version of this article.)

behavior of collagen-rich matrices. The results revealed that, rather than uniaxial deformation, the cells experienced both tensile (circumferential) and compressive (radial) strains, particularly near the PPyAu wire interface. These strains were mainly localized near the PPyAu wire interface and decreased monotonically with increasing radial distance (Fig. 3A-C).

To capture a more detailed mechanical behavior experienced by cells, strain was analyzed in terms of principal strains. The maximum principal strain (ε_max = ~14,800 με), corresponding approximately to circumferential stretching, exhibited a sharp peak at the actuator interface and decreased nonlinearly with distance. At a radial distance of 1000 μm, ε_max decreased to ~1177 με (~8% of interface strain), while at the biopsy punch boundary (2500 μm), ε_max was ~141 με (~1% of interface strain) (Fig. 3D). While 14,800 με would be considered pathophysiological or fracture-inducing in rigid, mineralized bulk bone in vivo, [15–17] it is widely established as a highly effective, physiological stimulus for cells cultured in vitro on compliant substrates. Conventional mechanobiology assays (e.g., Flexcell systems) routinely apply 1% to 5% strain (10,000 to 50,000 με) to overcome cell-substrate compliance and induce robust anabolic responses without causing apoptosis. [38,39] FEM analysis also predicted that only ~3.34% of the total membrane area, or 10.81% of the 5 mm biopsy region, experiences maximum principal strain above 1800 με (typical strain for an osteocyte to respond to mechanical loading), with this threshold reached at a radial distance of ~552 μm from the PPyAu wire surface.

In contrast, the minimum principal strain (ε_min), approximating radial deformation, exhibited a distinct spatial profile characterized by a strongly localized compressive deformation near the PPyAu wire interface. Immediately outside the actuator (r ≈ 270 μm), εr rapidly decreased, reaching a minimum of approximately −9500 με at ~100 μm from the PPyAu wire interface, then progressively diminished to ~ − 1200 με at ~1000 μm, further reducing to ~ − 400 με at the biopsy punch boundary and reaching near-zero values at a distance beyond 4100 μm (Fig. 3D, Suppl. Fig. 3).

Of note, sensitivity analysis based on the maximum principal strain was performed across broad ranges of collagen and cell-layer material properties and showed that despite these variations, the predicted spatial strain profile remained essentially unchanged. These findings indicate that the spatial attenuation of strain in this system is primarily defined by geometry and boundary conditions rather than by moderate changes in membrane material properties. These analyses also suggest that all cells collected within the biopsy punch boundary were subjected to a measurable degree of mechanical stimulation. Future studies, such as those employing spatial transcriptomics at single cell level, may further elucidate how these mechanical signals influence/activate responses in cells located at different distances from the actuation site.

3.2. *Localized micromechanical stimulations elicit distinct and cell-type-consistent transcriptional responses*

To investigate how cells rapidly translate mechanical cues into transcriptional outputs, we performed a systems-level analysis of early mechanosensitive gene regulation using RNA-seq datasets obtained from MC3T3-E1 and KUSA-A1 cells stimulated with the newly developed PPyAu wire actuator (Suppl. Fig. 4). Electrical activation of the electroactive PPy layer produced localized expansion of the actuator, thereby delivering defined micromechanical pressure directly onto the cell layer. Transcriptomes were collected at 30 min and 2 h post-stimulation to capture immediate-to-early phase transcriptional responses, immediately after the completion of the stimulation protocol. Differentially expressed genes (DEGs) common to both cell types and time points were used to construct gene regulatory networks.

To assess the transcriptional overlap between different stimulation modes, we generated Venn diagrams plotted in a table comparing the common DEGs across the two cell types (Table 1). Cyclic stimulation for 30 min (Cyc30) resulted in fewer DEGs, with no overlapped genes across the 2 cell types, when compared either with Cont1-NS or Cont2-UC. This indicates that Cyc30 is not enough to induce substantial changes in the total mRNA expression landscape in both cells, and suggests that the stimulus may have been absorbed or compensated at the mechanical, structural, and signaling levels before a robust gene-expression program was engaged. Notably, in the Cyc30/Cont1-NS comparison, MC3T3-E1 showed an upregulation of *Egr1*, a well-known immediate-early responsive gene, suggesting a faster and more sensitive response in this cell type.

On the other hand, Stat30 induced the upregulation of 11 and 76 genes in MC3T3-E1 cells and KUSA-A1 cells, respectively. When analyzed for the common DEGs across the two cells, 5 genes were commonly upregulated in both cell types (Tables 1 and 2, light blue cell). These results indicate that Stat30 evokes a broader and more consistent transcriptional program compared to the cyclic counterpart (Cyc30). Importantly, the transcriptional response of the immediate early genes *Fos*, *Btg2*, *Fosl1*, and *Egr1*, which are all well-established genes associated with mechanical stress, cytoskeletal tension, and substrate deformation, [40–42] supports the validity of the micromechanical stimulation system that we developed. In the Stat30/Cont1-NS comparison, although both cell types shared a core immediate-early mechanosensitive signature, KUSA-A1 displayed upregulation of numerous cell-cycle- and mitosis-related DEGs, indicating a stronger and more diverse transcriptional activation under Stat30 stimulation. On the other hand, in the Stat30/Cont2-UC comparison, MC3T3-E1 and KUSA-A1 displayed clearly distinct transcriptional profiles. MC3T3-E1 showed a relatively limited response, with upregulation of *Btg2*, and a passive tension/mechanosensing gene, *Ttn*, and several non-coding transcripts. By contrast, KUSA-A1 exhibited a broader response, with upregulated genes including *Ptgs2*, *Egr1*, and *Ibsp*, and many downregulated genes associated with extracellular matrix organization (e.g., *Col4a1*, *Fbn1*) and stromal identity (e.g., *Cxcl12*).

In addition, in each of the Stat30/Cont1-NS or Stat30/Cont2-UC comparisons, 1 uncharacterized long non-coding RNA (lncRNA: B930036N10Rik and 5430431A17Rik, respectively) was identified across both cell types, suggesting possible novel players in immediate-early mechanotransduction responses (Tables 1 and 2, light and dark blue cells). Because Cont1-NS controls for the PPy polymer without any actuation, and Cont2-UC controls for electrical stimulation without polymer-driven deformation, the fact that these DEGs emerge in both comparisons demonstrates that neither passive polymer contact nor pure electrical stimulation is sufficient to drive their expression. This indicates that the early transcriptional activation observed under Stat30 arises primarily from mechanical deformation generated by the PPyAu wire actuator, rather than from electrical stimulation. In the Cyc30/Stat30 comparison, both cell types showed only minimal transcriptional differences, suggesting that short-term cyclic and short static stimulations elicited similar adaptational responses. MC3T3-E1 exhibited just 2 DEGs corresponding to non-coding or uncharacterized transcripts (5430431A17Rik and D7Bwg0826e), and KUSA-A1 exhibited only 3 DEGs, all of which were lncRNA transcripts.

Prolonged cyclic stimulation (Cyc120) shifted both cell types toward stress-adaptative and repair-associated transcriptional program, as indicated by the upregulation in genes related to stress/antioxidant defense (*Hmox1*, *Gadd45b*) and ECM remodeling/angiogenesis (*Serpine1*), and feedback inhibition/termination of stress response (*Tnfaip3*, *Ski*) (Tables 1 and 2, light orange cells). Among the 3 genes (*Bhihe40*, *Gadd45b*, and *Serpine1*) identified in Cyc120/Cont2-UC (Tables 1 and 2, dark orange cells), two of them were also observed in Cyc120/Cont1-NS. In the Cyc120/Cont1-NS comparison, MC3T3-E1 exhibited mainly immediate-early and stress-responsive DEGs, including *Atf3*, *Fosb*, *Fosl1*, *Jun*, *Dusp4*, *Hmox1*, and *Tnfaip3*, while KUSA-A1 showed a broader response with a similar early-response core, but additionally displayed genes related to cell-cycle regulation, metabolism, and signaling, such as *Ccng2*, *Mdm2*, *Bhlhe40*, and *Srxn1*. A similar pattern was observed in Cyc120/Cont2-UC, where MC3T3-E1 showed a limited stress/adaptive

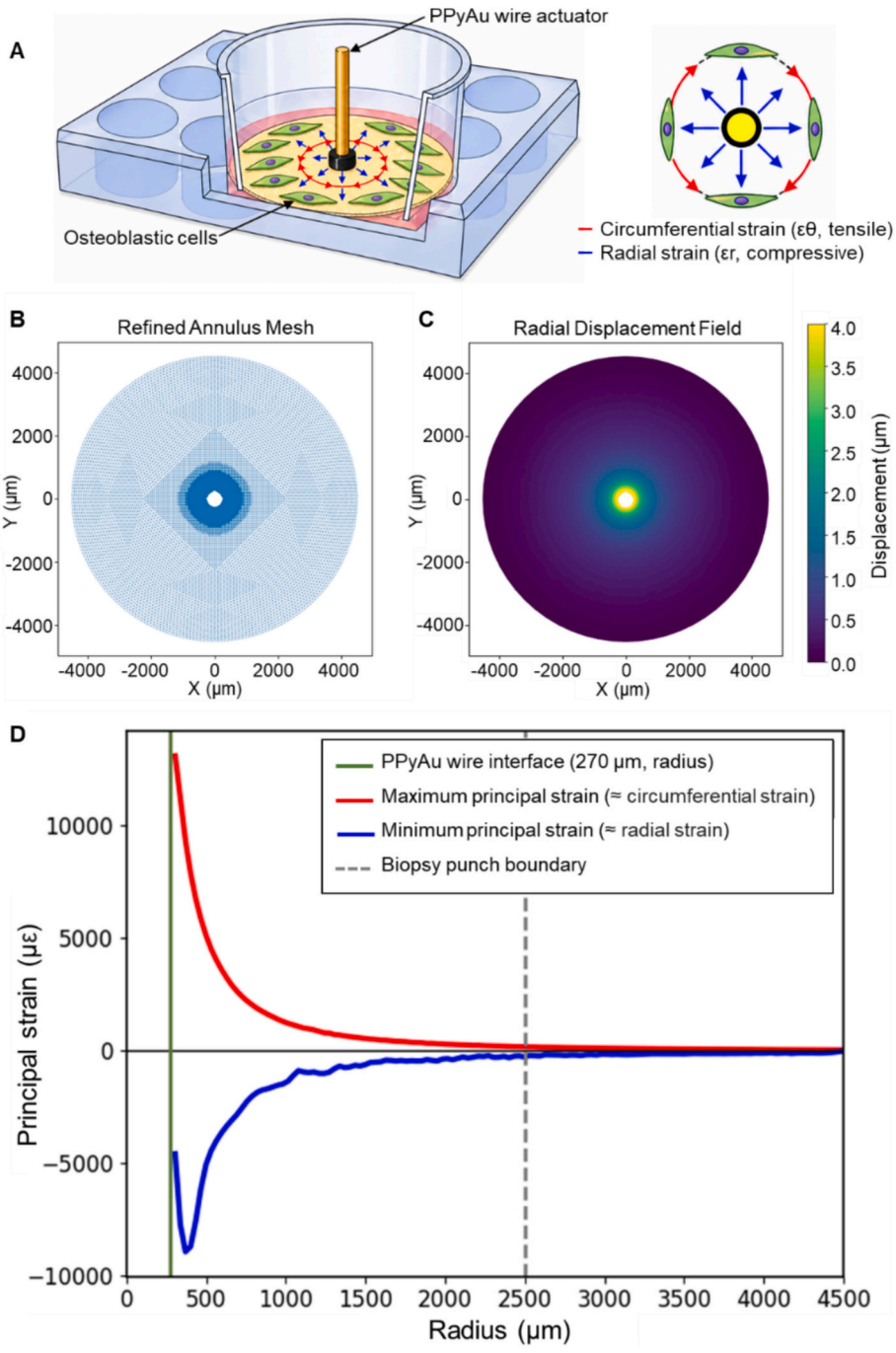

Fig. 3. Finite element analysis of actuator-induced displacement and principal strain components in the collagen membrane.
(A) Illustration showing the circumferential and radial strains.
(B) Refined finite element mesh of the annular computational domain representing the cell-seeded collagen membrane, with local mesh refinement (~50,000 triangular elements) near the PPyAu wire interface (inner radius: 270 μm) to accurately capture steep mechanical gradients. The outer boundary corresponds to an equivalent circular culture area of 64 mm^2 (4513 μm).
(C) Spatial distribution of radial displacement magnitude following actuator expansion (4 μm at the inner boundary). The displacement field is radially symmetric and decays smoothly with distance from the PPyAu wire interface, reaching submicron magnitudes beyond ~2000 μm.
(D) Radial profiles of in-plane principal strains as a function of distance from the actuator. The maximum principal strain (red line, ≈ circumferential strain) exhibits a nonlinear decay from a peak strain (~14,800 με) at the PPyAu wire interface (270 μm) to ~1177 με at 1000 μm (~8.0% of the interface strain), and to ~141 με (~0.95%) at the biopsy punch boundary (2500 μm). The minimum principal strain (blue line, ≈ radial strain) is highly compressive (~ − 9500) at 100 μm from the PPyAu wire interface, and gradually approaches ~ − 400 με at the biopsy punch boundary and near-zero values at a distance beyond 4100 μm. Dashed grey vertical line indicates the biopsy punch boundary. (For interpretation of the references to color in this figure legend, the reader is referred to the web version of this article.)

Table 1
Number of differentially expressed genes (DEGs) in response to micromechanical stimulation in both MC3T3-E1 and KUSA-A1 cells. The table summarizes the total number of upregulated (up) and downregulated (down) DEGs in MC3T3-E1 cells, KUSA-A1 cells, and the shared DEGs between both cell types across multiple stimulation conditions. Colored boxes indicate DEG counts for conditions in which shared transcriptional responses were detected in both cell lines.

	MC3T3-E1 (# DEGs)		KUSA-A1 (# DEGs)		MC3T3-E1 & KUSA-A1 (# common DEGs)	
	Up	Down	Up	Down	Up	Down
Cyc30 Vs Cont1-NS	1	1	1	0	0	0
Cyc30 Vs Cont2-UC	1	0	2	1	0	0
Stat30 Vs Cont1-NS	11	3	76	9	5	0
Stat30 Vs Cont2-UC	6	1	11	20	1	0
Cyc120 Vs Cont1-NS	21	2	34	4	8	0
Cyc120 Vs Cont2-UC	8	4	31	5	3	0
Cyc30 Vs Stat30	1	1	1	2	0	0
Cyc30 Vs Cyc120	13	4	36	10	4	0
Stat30 Vs Cyc120	2	0	34	8	1	0

response, while KUSA-A1 again displayed a broader and more functionally diverse transcriptional profile. When the Cyc120 was compared across the two control groups, MC3T3-E1 exhibited 7 shared DEGs out of 35 identified in the Cyc120/Cont1-NS and Cyc120/Cont2-UC comparisons, whereas KUSA-A1 exhibited 22 shared DEGs out of 74. For MC3T3-E1, genes unique to Cyc120/Cont1-NS included mostly those related to immediate-early mechanoresponse; whereas those unique to Cyc120/Cont2-UC were fewer and centered on *Bhlhe40* and *Txnip*, together with several non-coding/pseudogene transcripts. For KUSA-A1 cells, genes unique to Cyc120/Cont1-NS were related to RNA regulation/post-transcriptional control, antioxidant defense, apoptosis/stress survival, cell-cycle restraint, and additional transcriptional feedback regulation, while those unique to Cyc120/Cont2-UC were related to immediate-early signaling, energy metabolism, hypoxia/stress adaptation, and membrane/cytoskeletal or signaling-related remodeling.

Comparisons of short-term and prolonged stimulations revealed that in the Cyc30/Cyc120 condition, MC3T3-E1 displayed 17 DEGs largely reflecting a focused stress/adaptive program, whereas KUSA-A1 showed 46 DEGs encompassing stress-response, metabolic, hypoxia-related, and biomineralization-associated genes. The two cell types shared only a small core set of DEGs, including *Hmox1*, *Gadd45b*, *Serpine1*, and *Jun*. In contrast, in the Stat30/Cyc120 analysis, MC3T3-E1 showed almost no transcriptional difference (2 DEGs), whereas KUSA-A1 showed a substantial shift (42 DEGs), with genes associated with stress/adaptive, hypoxia-related, metabolic, and extracellular remodeling functions, including *Hmox1*, *Gadd45b*, *Tnfaip3*, *Hk2*, and *Serpine1*. Thus, the distinction between short-term and prolonged stimulations was more pronounced in KUSA-A1 than in MC3T3-E1.

It is worth to note that *Hmox1* was the only gene repeatedly observed across the Cyc30/Cyc120 (Tables 1 and 2, light green cells) and Stat30/Cyc120 regimens (Tables 1 and 2, dark green cells), suggesting its possible major role in the adaptation of cellular metabolism in response to either cyclic or static stress. The finding that *Hmox1* consistently appears as a differentially expressed gene across multiple comparisons involving the Cyc120 condition, including Cyc120/Cont1-NS, strongly indicates that *Hmox1* is a core molecular signature of prolonged cyclic mechanical stimulation. Unlike other genes whose presence depends on the comparison group, *Hmox1* is repeatedly detected in 120-min cyclic loadings, except when compared with Cont2-UC. Because *Hmox1* encodes heme oxygenase-1, a key regulator of oxidative stress adaptation and cytoprotection, its repeated induction indicates that Cyc120 imposes a sustained mechanical challenge that elevates cellular stress signaling, surpassing the levels triggered by either short-term cyclic (Cyc30) or static (Stat30) stimulations. Thus, *Hmox1* may serve as a robust and sensitive indicator of the intensity, duration, and cumulative load associated with prolonged cyclic mechanostimulation in osteoblast-like cells. These findings should, however, be validated in future work using time-matched controls (i.e., 120-min controls) to ensure that the observed changes are in fact driven by sustained mechanical actuation rather than cellular responses to the extended experimental duration.

It is also worth noting that a direct comparison between Cont1-NS and Cont2-UC revealed no overlapping DEGs in MC3T3-E1 and KUSA-A1 cells (data not shown), demonstrating that neither the electrical stimulus nor the PPy-DBS material itself significantly impacts the transcriptome without mechanical loading. This confirms that the observed gene expression changes are specifically driven by the radial expansion of the actuator.

3.3. Interactome analysis

Next, to further explore regulatory relationships among the DEGs, we conducted Bayesian causal network analysis of all upregulated mechanosensitive genes (Fig. 4A). This network depicts a transcriptional regulatory landscape centered around key transcription factors and co-factors inferred using Bayesian network analysis, with some interactions supported by ChIP-Seq data. Each node represents a gene, where the node color reflects its expression level (log2TPM), and each edge (arrow) represents a predicted or validated regulatory relationship. Solid lines denote relationships supported by ChIP-seq data, while dashed lines represent probabilistic inferences. The width and color of the edges represent the strength and causality of the interaction.

This approach revealed a hierarchical and highly structured network architecture, in which classical immediate-early transcription factors, including *Fos*, *Jun*, *Egr1*, *Fosl1*, and *Bhlhe40*, occupied the most central upstream positions, exhibiting the highest out-degree connectivity and strongest inferred causal influence. In particular, *Jun* and *Fos* family proteins are components of the AP-1 transcription factor complex, crucial in regulating genes involved in inflammation, cell cycle

Table 2
Differentially expressed genes (DEGs) and their annotations in response to micromechanical stimulation in both MC3T3-E1 and KUSA-A1 cells. The tables list the gene names, protein annotations, and functional descriptions of DEGs in both cells identified in Table 1. For Stat30/Cont1-NS, the shared upregulated DEGs include *Fos*, *Btg2*, *Fosl1*, and *Egr1*, all known early-response transcription factors, along with one uncharacterized gene. For Stat30/Cont2-UC, 5430431A17Rik was the only DEG detected. For Cyc120/Cont1-NS, multiple DEGs were identified, including key stress- and apoptosis-related genes (*HMOX1*, *GADD45b*, *Serpine1*, *Fosl1*, *Jun*, *Skil*, *Tnfaip3*, *Fosb*). In Cyc120/Cont2-UC, the upregulated DEGs included *Bhlhe40*, *Serpine1*, and *Gadd45b*. The Cyc30/Cyc120 comparison highlights genes consistently activated during prolonged loading, including *HMOX1*, *Gadd45b*, *Serpine1*, and *Jun*. For the Stat30/Cyc120 comparison, only Hmox1 was detected as a conserved gene in both cell types.

Stat30 Vs Cont1-NS		
Gene Name	**Protein Name**	**Gene Annotation**
B930036N10Rik	Uncharacterized	Unknown
Fos	c-Fos	Nuclear phosphoprotein which forms a complex with JUN/AP-1
Btg2	BTG2	Transcription corepressor
Fosl1	Fos-related antigen 1	Transcription factor
Egr1	Early growth response protein 1	Transcription factor

Stat30 Vs Cont2-UC		
Gene Name	**Protein Name**	**Gene Annotation**
5430431A17Rik	Uncharacterized	Unknown

Cyc120 Vs Cont1-NS		
Gene Name	**Protein Name**	**Gene Annotation**
Fosb	FosB	Transcription factor
Serpine1	Plasminogen activator inhibitor 1	ECM remodeling, angiogenesis, cellular response to TGF-β
Hmox1	Heme oxygenase 1	Oxidative stress response, cytoprotection
Gadd45b	Growth arrest and DNA damage-inducible protein GADD45 beta	Apoptotic process
Fosl1	Fos-related antigen 1	Transcription factor
Jun	Transcription factor Jun	Transcription factor
Skil	Ski-like protein	Transcription repressor
Tnfaip3	Tumor necrosis factor alpha-induced protein 3	Cysteine-type deubiquitinase activity, DNA binding

Cyc120 Vs Cont2-UC		
Gene Name	**Protein Name**	**Gene Annotation**
Bhlhe40	Class E basic helix-loop-helix protein 40	Transcription factor
Serpine1	Plasminogen activator inhibitor 1	ECM remodeling, angiogenesis, cellular response to TGF-β
Gadd45b	Growth arrest and DNA damage-inducible protein GADD45 beta	Apoptotic process

Cyc30 Vs Cyc120		
Gene Name	**Protein Name**	**Gene Annotation**
Hmox1	Heme oxygenase 1	Oxidative stress response, cytoprotection
Gadd45b	Growth arrest and DNA damage-inducible protein GADD45 beta	Apoptotic process
Serpine1	Plasminogen activator inhibitor 1	ECM remodeling, angiogenesis, cellular response to TGF-β
Jun	Transcription factor Jun	Transcription factor

Stat30 Vs Cyc120		
Gene Name	**Protein Name**	**Gene Annotation**
Hmox1	Heme oxygenase 1	Oxidative stress response, cytoprotection

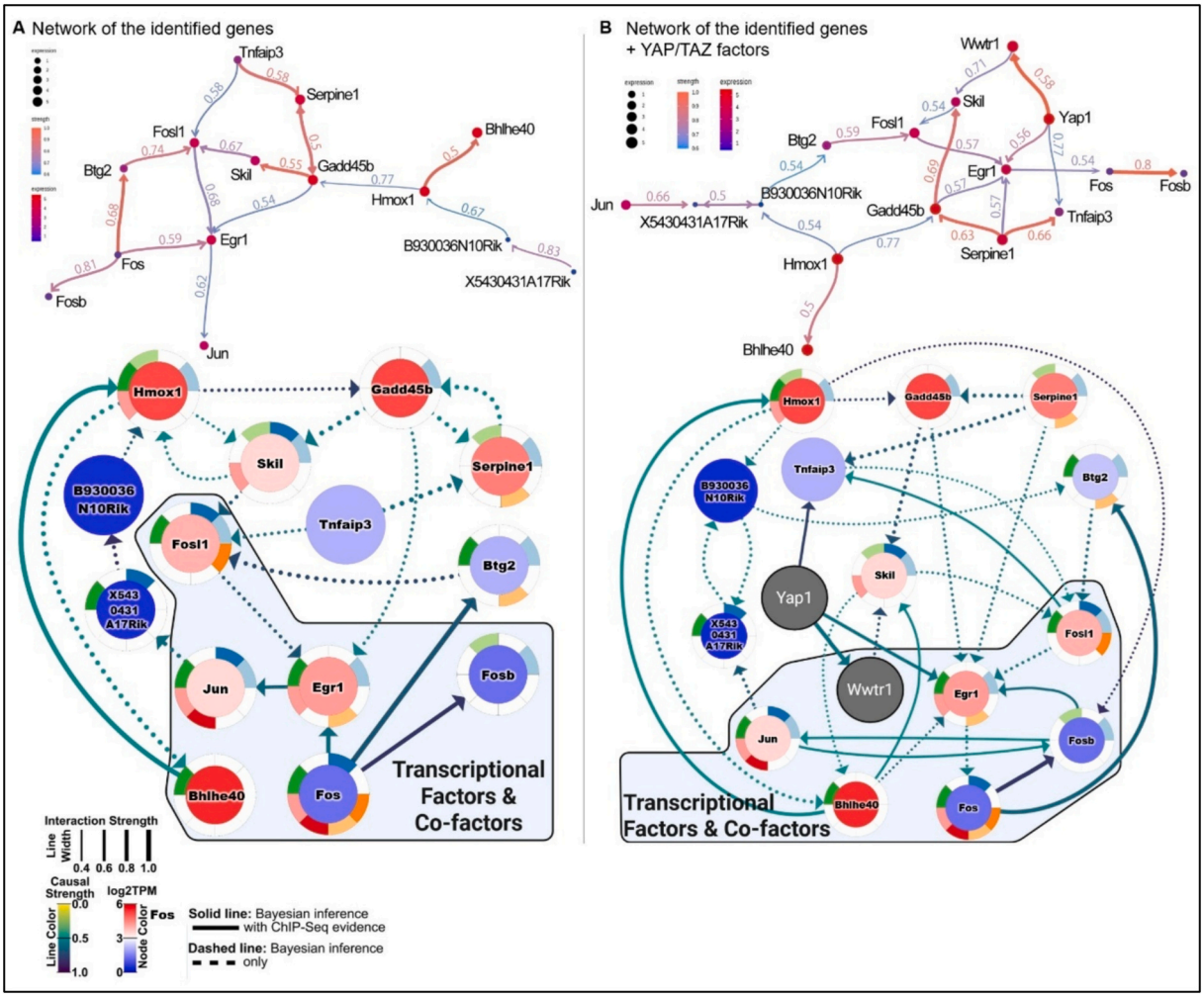

Fig. 4. Interactome analysis of mechanosensitive genes in response to micromechanical stimulation. This integrative network diagram illustrates the inferred regulatory relationships among the DEGs in response to mechanical stimulation, constructed using Bayesian network inference, ChIP-seq evidence, and RNA-seq expression data. Nodes (genes) are color-coded by expression level (log_2TPM), ranging from low (blue) to high (red), and the size of the nodes reflects relative expression magnitude. Edges (arrows) represent inferred regulatory relationships. Solid lines indicate relationships supported by both Bayesian inference and ChIP-seq data. Dashed lines indicate predictions from Bayesian inference only. Line color represents the inferred causal strength of the interaction (green to red, with red being strongest). Line width corresponds to interaction strength (thicker lines indicate stronger regulatory influence). (A) Prominent transcriptional regulators such as *Fos*, *Jun*, *Egr1*, and *Fosl1* occupy central network positions, coordinating broad regulatory responses. Notably, *Hmox1* and *Gadd45b* appear as key downstream effectors with strong expression, implicating them in stress response and cytoprotection. At the bottom, the group of transcription factors and co-factors (*Fos*, *Jun*, *Egr1*, *Fosl1*, *Bhlhe40*), which likely initiate or modulate the transcriptional response are highlighted. Genes such as *Hmox1*, *Skil*, and *Gadd45b* are connected via multiple dotted arrows, indicating their role as integrative hubs in downstream processes. Peripheral genes such as *Skil*, *Tnfaip3*, and *Serpine1* integrate multiple regulatory signals, while *B930036N10Rik* and *X5430431A17Rik* emerge as strongly upregulated but less-characterized components of the network. This visualization emphasizes the coordinated induction of transcriptional programs involving immediate-early response genes, stress regulators, and putative novel mechanosensitive genes in response to mechanical cues. (B) Network topology map of mechanosensitive genes identified in this study, in association with the well-known and YAP/TAZ-associated mechanosensitive genes. Key regulators such as *Fos*, *Fosb*, *Egr1*, *Jun*, *Bhlhe40*, and *Tnfaip3* continue to be central to mechanotransduction together with YAP/TAZ-related genes. *Yap1* shows strong regulatory links to *Tnfaip3* and *Erg1* mechanoregulatory genes, while *Wwtr1* is linked to *Skil*. (For interpretation of the references to color in this figure legend, the reader is referred to the web version of this article.)

progression, and apoptosis. Another key transcription factor, Egr1, integrates signals from Yap1/Wwtr1 [43] and further modulates AP-1 components and downstream targets such as *Fosb* and *Skil*. These transcription factors formed the core regulatory module, rapidly activated within 30 min, and propagated downstream signals toward stress-responsive and redox-regulating genes such as *Hmox1*, *Gadd45b*, and *Serpine1*, localized on the periphery of the network. These genes are also involved in DNA damage repair, inflammation regulation, and inhibition of apoptosis, reflecting an activated cellular state under stress or injury.

Consistently, nodes representing *Hmox1* and *Gadd45b* appeared in distal downstream positions with large node sizes and intense red coloration, reflecting strong transcriptional activation (log_2TPM), while their lower outgoing edge count suggested their primary role as effector genes rather than regulators. Genes such as *Skil*, *Btg2*, *Tnfaip3*, and *Serpine1* formed intermediate layers within the network, mediating signal propagation between early transcription factors and stress-related effectors, and displaying multiple bidirectional or converging edges that indicate their integrative roles.

While Bayesian network inference (Fig. 4B) is primarily data-driven and captures statistical dependencies between gene expression profiles, it may not inherently account for master regulators like YAP/TAZ, whose activity is largely governed by nuclear translocation and post-translational modification rather than immediate mRNA fluctuations, especially in short-time experimental setups. In fact, YAP/TAZ was not experimentally identified as DEGs in this study. Consequently, in

addition to the Bayesian inference analysis using only the modulated genes identified herein, we integrated Yap1 and Wwtr1 (TAZ) as biologically informed nodes within the network. Although still uncommon, this hybrid approach combining data-driven gene dependencies with established regulatory anchors, positioned YAP/TAZ as upstream regulators of several modulated genes, consistent with their well-documented roles as primary mechanotransducers.

In our model, Yap1 showed predicted regulatory influence on *Egr1*, *Fosl1*, *Skil*, and *Tnfaip3*, while *Wwtr1* connected to *Jun* and *Bhlhe40*, thereby forming a prolonged mechanotransduction module. This integration led to an increased density of regulatory edges connecting YAP/TAZ to downstream stress effector genes such as *Hmox1*, *Gadd45b*, and *Serpine1*, suggesting that YAP/TAZ may amplify or coordinate transcriptional responses initiated by immediate-early transcription factors. Downstream of Yap1/Wwtr1 are canonical transcription factors, including *Jun*, *Egr1*, *Fos*, *Fosb*, and *Bhlhe40*, that facilitate rapid responses in stress, immune signaling, and cell fate decisions. The two uncharacterized lncRNAs, *B930036N10Rik* and *X5430431A17Rik*, were consistently upregulated and positioned downstream of transcription factor hubs in both network models. Although lacking prior mechanobiological annotation, these genes received regulatory inputs from early transcription factors, indicating potential roles as novel mechanosensitive genes.

Collectively, this extended network analysis allowed the visualization of a hierarchical regulatory structure where *Yap1* and *Wwtr1* function as upstream master regulators, activating a cascade of transcription factors (e.g., *Jun*, *Egr1*, *Fos* family) that, in turn, control expression of genes critical for stress response, inflammation, and cell survival. The integration of causal strength, interaction evidence, and gene expression levels still needs further probatory evidence, but provides a more comprehensive view of the immediate-early transcriptional control mechanisms within this biological system.

3.4. Global overview of GO biological processes

To elucidate the biological significance of transcriptomic alterations induced by micromechanical stimulations, we performed Gene Ontology Biological Process (GO-BP) enrichment analyses to identify conserved processes across both MC3T3-E1 and KUSA-A1 cells (Table 3, Suppl. Figs. 5–10). This analysis was conducted independently of the list of overlapping DEGs identified in Tables 1 and 2. GO-BP terms that were significantly enriched in both cell types were considered representative of shared mechanotransductive pathways. Comparisons were made among cyclic (Cyc30, Cyc120), static (Stat30), and control (Cont1-NS, Cont2-UC) conditions to distinguish immediate and early mechanobiological responses.

As shown in Table 3 (right cells), neither the Cyc30 nor the Stat30 conditions produced substantial changes in enriched GO-BP signatures. Only one GO-BP was down-regulated in Stat30/Cont1-NS (Suppl. Fig. 9), suggesting that prolonged stimulations are necessary to drive significant cellular responses. Indeed, a markedly higher number of enriched GO-BPs was observed under prolonged Cyc120 stimulation regimens. In the Cyc120/Cont1-NS and Cyc120/Cont2-UC, 32 and 18 GO-BPs were respectively upregulated, and modulated a distinct set of processes associated with cellular adaptation, although with lower overall pathway diversity, indicating a shift from acute signaling to sustained remodeling activity. The two GO-BPs common to both Cyc120/Cont1-NS and Cyc120/Cont2-UC were "regulation of extrinsic apoptotic signaling pathway via death domain receptors" and "regulation of protein maturation" (Suppl. Figs. 5, 6). The first pathway controls cell survival decisions mediated by external mechanical or biochemical cues, i.e., under prolonged mechanical loading, cells may experience mechanical strain, membrane deformation, oxidative stress, or cytoskeletal tension, all of which can activate death-domain receptor signaling (e.g., TNFR, FAS). In other words, the activation of this pathway suggests that cells are actively modulating apoptosis-related signals to avoid cell death, and they engage protective and homeostatic mechanisms to maintain viability under prolonged mechanical load. On the other hand, activation of "regulation of protein maturation" GO-BP suggests that cells are remodeling their proteome in response to sustained mechanical cues, and preparing functional proteins necessary for cytoskeletal remodeling, adhesion, stress adaptation, and mechanotransduction. These findings align well with the observed upregulation of *Gadd45b* and *Hmox1*, both of which are known survival- and stress-mitigation genes. [44–47] Moreover, *Serpine1* is involved in the regulation of proteolytic cascades and protein activation/maturation processes during tissue remodeling, and *Tnfaip3* influences ubiquitin-dependent processing and maturation of signaling proteins, particularly within NF-κB and inflammatory pathways.

The larger number and greater diversity of pathways in Cyc120/Cont1-NS indicate that the PPyAu wire actuator under cyclic actuation evokes a more complex, multilayered adaptive response encompassing stress regulation, extracellular-matrix (ECM) remodeling, and angiogenesis. The GO enrichment network derived from the Cyc120/Cont1-NS comparison revealed a dense cluster of processes associated with stress and apoptotic signaling, including "regulation of extrinsic apoptotic signaling pathway via death domain receptors", "cellular response to oxidative stress", "response to wounding", and "negative regulation of inflammatory response" (Suppl. Fig. 5). Core genes involved in these networks—*Hmox1*, *Gadd45b*, *Jun*, *Fos*, *Fosl1*, *Serpine1*, and *Tnfaip3*—represent canonical components of early response transcriptional circuits. Notably, the AP-1 transcriptional complex (*Fos*, *Jun*, *Fosl1*) and its regulators were consistently enriched in GO terms related to signal transduction and transcriptional activation, suggesting that cyclic stimulation rapidly initiates mechano-transductive gene networks. *Hmox1* and *Gadd45b*, both known mediators of oxidative stress adaptation and DNA repair, were found at the intersection of multiple enriched GO-BPs, reinforcing their central role in cytoprotective and remodeling mechanisms during the early phase of stimulation. [48]

In contrast, the Cyc120/Cont2-UC network exhibited a smaller but focused topology comprising 18 enriched GO-BPs, centered on oxidative stress defense, proteostasis, and circadian/metabolic regulation (Suppl. Fig. 6). Major terms included regulation of apoptotic signaling, regulation of protein maturation, vascular development, and entrainment of the circadian clock. Key contributors were *Bhlhe40*, *Hmox1*, *Gadd45b*, and *Serpine1*. Bhlhe40 is a circadian transcription factor that responds to rhythmic mechanical or metabolic cues, suggesting that repetitive deformation imposes a temporal transcriptional rhythm. Notably, these genes remained responsive even when the electrical potential was applied to an uncoated Au wire, confirming that mechanical deformation of the PPyAu wire actuator—not the electrical current—is the essential trigger for these adaptive pathways.

The GO-BP networks also revealed that distinct biological programs are activated when short-duration stimulations (Cyc30 or Stat30) are compared to prolonged cyclic stimulation (Cyc120), highlighting how osteoblast-like cells differentially sense mechanical duration and pattern (Suppl. Figs. 7, 8). The Cyc30/Cyc120 comparison shows upregulation of a broad and heterogeneous set of biological processes, driven by genes such as *Btg2*, *Jun*, *Tnfaip3*, *Serpine1*, *Gadd45a*, *Adm*, *Vegfa*, and *Hk2*. These genes cluster into several major functional themes: Vascular and angiogenic regulation (*Vegfa*, *Adm*), suggesting a transient, early "pro-regenerative" or pro-angiogenic response under shorter cyclic loading. Cellular stress and metabolic adaptation (*Hk2*, *Gadd45a*, *Tnfaip3*) reflect acute responses to rapid but short-lived mechanical strain (Suppl. Fig. 7). Regulation of fibroblast proliferation and wound healing (*Serpine1*, *Skil*) indicates remodeling signals triggered by brief but repetitive deformation. Immune and inflammatory modulation (*Tnfaip3*, *Btg2*), suggesting that short cyclic loading may engage early inflammatory regulatory pathways. Smooth muscle and keratinocyte-associated processes possibly reflecting cytoskeletal and contractility adjustments in response to short mechanical pulses. Overall, Cyc30 induces a wide-ranging, multi-system early mechanosensitive program, whereas

Cyc120 produces a response and adaptation to stress. Three GO-BPs were found to be downregulated in the Cyc30/Cyc120 comparison (Suppl. Fig. 10). These GO-BPs encompass genetic programs required for nephrogenesis, including ureteric bud branching, nephron formation, and maturation of renal cell types.

In the Stat30/Cyc120 comparison, a more focused oxidative stress–autophagy axis can be observed (Suppl. Fig. 8). In contrast to that of Cyc30/Cyc120, the enriched GO-BPs of Stat30/Cyc120 network fall into a coherent set of processes: Oxidative stress response and cyto-protection (*Hmox1*) highlighting oxidative-mechanical stress as a key feature differentiating Stat30 from prolonged cyclic loading. Regulation of apoptosis and epithelial apoptotic pathways (*Tnfaip3*, *Mdm2*), suggesting that static deformation activates controlled cell-survival and damage-prevention pathways. Autophagy and macroautophagy regulation (*Ulk1*, *Bnip3*) indicate engagement of cellular recycling programs in response to static indentation. Cell migration and epithelial remodeling (*Gpi1*, *Serpine1*) reflect tissue-remodeling cues triggered by mechanical compression.

Together, these results reveal that Cyc30 activates diverse biological pathways, including angiogenesis, immune modulation, and early wound-healing signals, whereas Stat30 activates a tighter stress-response program centered on oxidative stress, apoptosis regulation, and autophagy. In contrast, Cyc120 induces a more potent mechanical stress signature that suppresses many of these early transient programs, leading to consistent upregulation of stress-protective genes such as *Hmox1*. These GO-BP patterns underscore how osteoblast-like cells can discriminate between mechanical pattern and duration, activating distinct mechanotransductive pathways that likely correspond to different physiological roles in bone remodeling and adaptation.

3.5. *Identified genes are enriched for mechanotransduction- and stress-associated pathways based on literature mining*

Finally, to contextualize the functional relevance of the DEGs, we performed literature-based enrichment analysis using curated keyword searches. Specifically, we examined the association of DEGs with biological concepts including “mechanotransduction,” “mechanical phenomena,” “stress,” and combinations of these terms with “osteoblast” to assess cell-type relevance.

Among the DEGs identified under cyclic stimulation, several genes were found to be strongly associated with the keyword “mechanotransduction” in the literature (Fig. 5A, left panel). Notably, *Fosb* and *Egr1* showed statistically significant enrichment, with *Egr1* displaying the highest relevance (log2(*p*-value) > 10). These genes are well-characterized early response transcription factors involved in cellular responses to mechanical and biochemical signals. However, when we analyzed the association of DEGs specifically with“Osteoblast” and “Mechanotransduction”, no gene was identified (Fig. 5A, right panel).

Further analysis using the term “stress” revealed enrichment of additional DEGs such as *Gadd45b*, *Hmox1*, *Jun*, *Fos*, *Egr1*, and *Btg2* (Fig. 5B, left panel). Of particular interest, *Hmox1* demonstrated the strongest enrichment, suggesting a robust cellular stress response component. When filtered with “osteoblast” and “stress”, *Hmox1* remained significantly enriched (Fig. 5B, right panel), suggesting its critical role in mechanical stress adaptation in osteoblasts, as was also indicated by our experiments (Table 2).

A substantial proportion of DEGs exhibited significant literature associations with “apoptosis” (Fig. 5C, left panel). Prominently, *Jun*, *Egr1*, *Fos*, *Tnfaip3*, *Gadd45b*, *Hmox1*, *Btg2*, *Fosb*, and *Serpine1* were enriched, suggesting that mechanical perturbation may initiate apoptotic signaling cascades. These genes are commonly reported as immediate-early genes and stress-responsive regulators implicated in programmed cell death, particularly under conditions of mechanical and oxidative stress. When filtered with “osteoblast” and “apoptosis”, *Jun* emerged as the most relevant DEG (Fig. 5C, right panel), indicating that mechanical stimulation may trigger apoptotic regulation specifically in osteogenic lineages.

We also identified several DEGs significantly associated with “autophagy” (Fig. 5D, left panel), including *Hmox1*, *Tnfaip3*, *Egr1*, *Jun*, *Skil*, and *Bhlhe40*. These genes have been previously implicated in autophagy regulation in response to oxidative stress or cytokine signaling. Notably, *Hmox1* and *Tnfaip3* showed the highest enrichment, supporting the hypothesis that autophagic responses are also engaged by the mechanical environment induced through the micromechanical stimulation system that we have developed. However, the intersectional analysis with “osteoblast” and “autophagy” revealed no overlap (Fig. 5D, right panel), suggesting that while autophagy-related genes are activated, their direct functional annotation in osteoblasts is less well established in the current literature.

Collectively, these literature mining results provide compelling evidence that the genes modulated by the electrically-driven

Table 3
Gene Ontology Biological Process (GO-BP) responses to micromechanical stimulation in MC3T3-E1 and KUSA-A1 cells. (A) Summary table of enriched GO-BPs identified from DEGs in MC3T3-E1 cells, KUSA-A1 cells, and shared DEGs between the two cell types, analyzed independently of the DEGs identified in Table 1. Substantial enrichment was observed after prolonged stimulation, Cyc120, compared to either Cyc30, Stat30, C1-NC, or Cont2-UC, in both MC3T3-E1 and KUSA-A1. Down-regulated GO-BPs were related to catabolic carbohydrate process and kidney and renal development.

	MC3T3-E1 (GO-BPs)		KUSA-A1 (GO-BPs)		MC3T3-E1 & KUSA-A1 (GO-BPs)	
	Up	Down	Up	Down	Up	Down
Cyc30 Vs Cont1-NS	141	0	0	0	0	0
Cyc30 Vs Cont2-UC	0	0	50	0	0	0
Stat30 Vs Cont1-NS	158	480	357	110	0	1
Stat30 Vs Cont2-UC	86	0	273	429	0	0
Cyc120 Vs Cont1-NS	642	0	459	7	32	0
Cyc120 Vs Cont2-UC	169	16	473	14	18	0
Cyc30 Vs Stat30	0	0	0	0	0	0
Cyc30 Vs Cyc120	545	185	416	54	48	3
Stat30 Vs Cyc120	167	0	443	45	21	0

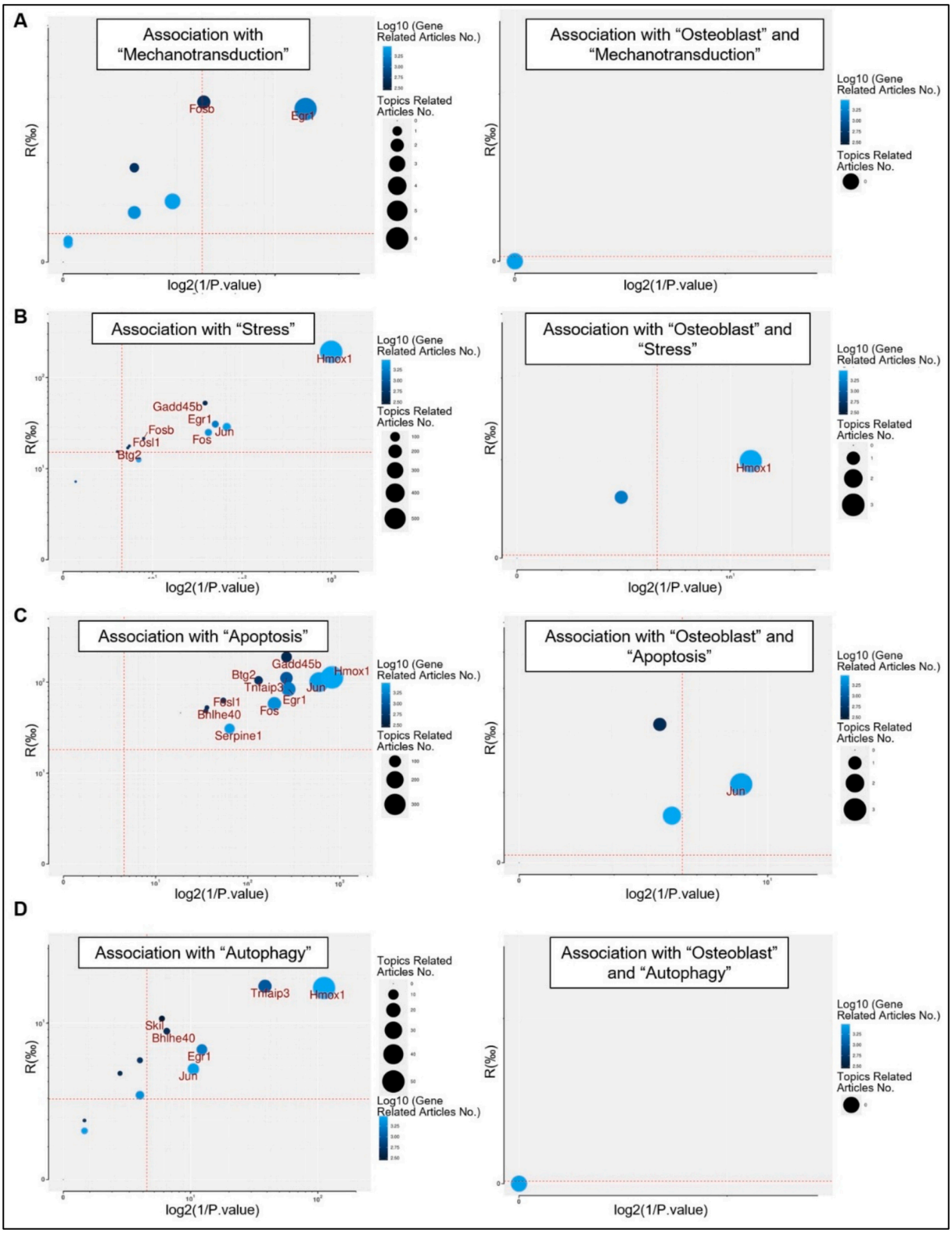

(caption on next page)

Fig. 5. Literature mining analysis: association of genes identified in RNA-seq with the keywords: (A) "Mechanotransduction", (B) "Stress", (C) "Apoptosis", and (D) "Autophagy", in a broad search or specifically in "Osteoblast". The x-axis represents the -log2(*p*-value), and the y-axis indicates the R score (% relevance in topic-specific articles). Red dashed lines indicate the thresholds for statistical significance (log_2(1/P)) and literature relatedness (R), effectively isolating key mechanosensitive candidates in the upper-right quadrant. Genes with R values above 10 K/N and FDR or *P*-value (if K ⟨100) lower than 0.05 were considered significant. Bubble size reflects the number of related articles. (A) Association of DEGs with "Mechanotransduction" (left) and with combined "Osteoblast" + "Mechanotransduction" terms (right). Immediate early genes such as *Fos* and *Egr1* show modest mechanotransduction-related associations, but no DEGs demonstrate combined osteoblast-mechanotransduction relevance. (B) Association of DEGs with "Stress" (left) and with combined "Osteoblast" + "Stress" terms (right). Multiple DEGs—including *Gadd45b*, *Fos*, *Fosl1*, *Jun*, *Btg2*, and *Egr1*—cluster around stress-related topics, with *Hmox1* showing the strongest and most specific association. Only *Hmox1* demonstrates a detectable link to both osteoblast biology and stress response. (C) Association of DEGs with "Apoptosis" (left) and with combined "Osteoblast" + "Apoptosis" terms (right). Numerous DEGs display strong connections to apoptotic processes, including *Hmox1*, *Gadd45b*, *Tnfaip3*, *Bhlhe40*, *Serpine1*, and *Jun*. Among them, *Jun* is the only gene exhibiting a detectable co-association with osteoblast biology and apoptosis. (D) Association of DEGs with "Autophagy" (left) and with combined "Osteoblast" + "Autophagy" terms (right). Genes such as *Hmox1*, *Tnfaip3*, *Bhlhe40*, *Skil*, and *Jun* demonstrate varying degrees of association with autophagy-related pathways. No DEGs show a significant combined association with osteoblast biology and autophagy. (For interpretation of the references to color in this figure legend, the reader is referred to the web version of this article.)

micromechanical stimulation system that we have developed are consistent with the reported literature. This substantiates the physiological relevance of the stimulation strategy and highlights *Fos*, *Jun*, *Egr1*, and *Hmox1* as key immediate-early mechano-responsive genes. Details of the PubMed retrieved queries and other related results can be found in the Suppl. Table 1 as well as at: http://ppybcell.bs-gou.com.

4. Conclusion

In this study, we developed and validated a novel electrically driven PPy-based wire actuator capable of delivering precise, localized micromechanical stimuli to osteoblast-like cells (MC3T3-E1 or KUSA-A1). The PPyAu wire actuator could deliver short-term (30 min) cyclic (Cyc30) or static (Stat30) micromechanical stimulations, as well as prolonged (120 min) cyclic (Cyc120) stimulation, of ~4 μm radial expansion to the cells seeded on a cell insert. By integrating this platform with high-resolution transcriptomic and computational network analyses, we systematically identified immediate-early mechanosensitive genes and mapped the biological processes underlying acute and sustained mechanoadaptation. Short-term loading (Cyc30, Stat30) selectively activated canonical early-response transcription factors—including *Fos*, *Jun*, *Egr1*, *Fosl1*, and *Btg2*—supporting the fidelity of the stimulation system and confirming conserved mechanotransductive mechanisms across both MC3T3-E1 and KUSA-A1 cells. In contrast, Cyc120 induced a robust stress-adaptation transcriptional program, consistently upregulating key cytoprotective and DNA-damage–responsive genes such as *Hmox1* and *Gadd45b*. Among these, *Hmox1* emerged as the most reproducible signature of sustained cyclic deformation, suggesting its essential role in oxidative stress adaptation during prolonged mechanical challenge.

GO-BP enrichment analyses revealed clear distinctions between mechanical regimens: short-term loading broadly activated immune-like and angiogenic pathways, whereas sustained cyclic loading elicited oxidative stress, apoptosis-regulation, circadian, and protein-maturation pathways. Bayesian gene regulatory network modeling further demonstrated that immediate-early transcription factors form the central regulatory core of the mechanotransductive response, with downstream effector genes mediating stress mitigation and survival. Incorporation of YAP/TAZ into network inference highlighted their potential upstream modulatory roles, linking classical mechanosensors to the early transcriptional cascade. Our results demonstrate that the developed micromechanical stimulation system is a useful tool for mechanobiology. These findings provide an integrative framework for understanding how osteoblasts sense mechanical cues at the microscale and translate them into coordinated transcriptional programs, offering valuable insights for bone biology, regenerative medicine, and mechanotherapy design.

CRediT authorship contribution statement

Jiamin Chen: Writing – original draft, Resources, Investigation, Formal analysis, Data curation. **Amaia B. Ortega-Santos:** Writing – original draft, Resources, Methodology, Investigation, Formal analysis, Data curation. **Satoru Hayano:** Writing – original draft, Resources, Methodology, Investigation, Formal analysis. **Ziyi Wang:** Writing – original draft, Visualization, Software, Formal analysis. **Jose G. Martinez:** Writing – original draft, Visualization, Methodology, Investigation, Formal analysis, Conceptualization. **Emilio Satoshi Hara:** Writing – review & editing, Writing – original draft, Visualization, Validation, Supervision, Software, Project administration, Methodology, Funding acquisition, Formal analysis, Data curation, Conceptualization. **Edwin W.H. Jager:** Writing – review & editing, Writing – original draft, Supervision, Resources, Project administration, Methodology, Funding acquisition, Data curation, Conceptualization. **Hiroshi Kamioka:** Writing – review & editing, Supervision, Methodology, Funding acquisition, Conceptualization.

Declaration of competing interest

The authors declare that they have no known competing financial interests or personal relationships that could have appeared to influence the work reported in this paper.

Data availability

The original datasets used in the RNA-seq analysis can be accessed at the National Center for Biotechnology Information, archived under Gene Expression Omnibus accession code GSE314317.

Acknowledgements

This work was partially supported by JSPS KAKENHI Grant Numbers JP23K27804 and JP23KK0163, and bilateral joint research project grant by JSPS (JPJSBP120209923). The authors thank Mitsuaki Ono for his support in the bioinformatic analysis. ABOS, JGM & EWHJ acknowledge the support from the bilateral joint research project grant by STINT, The Swedish Foundation for International Cooperation in Research and Higher Education (MG2019-8171), and from the Swedish Research Council (VR2019-03658). EWHJ acknowledges the financial support from the Swedish Government Strategic Research Area in Materials Science on Functional Materials at Linköping University (Faculty Grant SFO-Mat-LiU No. 2009 00971), Scandinavia-Japan Sasakawa Foundation (GA24-SWE-0081), and JSPS (BR170502 and S25156).

Appendix A. Supplementary data

Supplementary data to this article can be found online at https://doi.org/10.1016/j.bone.2026.117914.

References

[1] B. Xiao, Mechanisms of mechanotransduction and physiological roles of PIEZO channels, Nat. Rev. Mol. Cell Biol. 25 (11) (2024) 886–903.

[2] R. Yan, Y. Li, S. Chen, L. Zhu, C. Zhou, J. Chen, S. Zou, X. Han, Mechanotransduction in shaping immunity: pathways, crosstalk, and pathophysiological relevance, Adv. Sci. (Weinh.) 12 (41) (2025) e12164.
[3] X. Di, X. Gao, L. Peng, J. Ai, X. Jin, S. Qi, H. Li, K. Wang, D. Luo, Cellular mechanotransduction in health and diseases: from molecular mechanism to therapeutic targets, Signal Transduct. Target. Ther. 8 (1) (2023) 282.
[4] B. Javaheri, A.A. Pitsillides, Aging and mechanoadaptive responsiveness of bone, Curr. Osteoporos. Rep. 17 (6) (2019) 560–569.
[5] B. Yu, C.Y. Wang, Osteoporosis and periodontal diseases - an update on their association and mechanistic links, Periodontol 2000 89 (1) (2022) 99–113.
[6] L. Wang, X. You, L. Zhang, C. Zhang, W. Zou, Mechanical regulation of bone remodeling, Bone Res. 10 (1) (2022) 16.
[7] R.L. Duncan, C.H. Turner, Mechanotransduction and the functional response of bone to mechanical strain, Calcif. Tissue Int. 57 (5) (1995) 344–358.
[8] S. Bolamperti, I. Villa, A. Rubinacci, Bone remodeling: an operational process ensuring survival and bone mechanical competence, Bone Res. 10 (1) (2022) 48.
[9] T. Adachi, Y. Aonuma, K. Taira, M. Hojo, H. Kamioka, Asymmetric intercellular communication between bone cells: propagation of the calcium signaling, Biochem. Biophys. Res. Commun. 389 (3) (2009) 495–500.
[10] T. Ishimoto, K. Kawahara, A. Matsugaki, H. Kamioka, T. Nakano, Quantitative evaluation of osteocyte morphology and bone anisotropic extracellular matrix in rat femur, Calcif. Tissue Int. 109 (4) (2021) 434–444.
[11] K. Li, Y.N. Jan, Experimental tools and emerging principles of organellar mechanotransduction, Trends Cell Biol. 31 (11) (2025) 944–954.
[12] D.E. Ingber, N. Wang, D. Stamenovic, Tensegrity, cellular biophysics, and the mechanics of living systems, Rep. Prog. Phys. 77 (4) (2014) 046603.
[13] D.E. Ingber, Tensegrity-based mechanosensing from macro to micro, Prog. Biophys. Mol. Biol. 97 (2–3) (2008) 163–179.
[14] J. Rowe, S.B.A. Shen, A.C.S. de Alcântara, M.S. Skaf, D. Dini, N.M. Harrison, U. Hansen, M.J. Buehler, R.L. Abel, Integrating computational and experimental advances in bone multiscale mechanics, Prog. Mater. Sci. 153 (2025).
[15] X. Li, L. Han, I. Nookaew, E. Mannen, M.J. Silva, M. Almeida, J. Xiong, Stimulation of Piezo1 by mechanical signals promotes bone anabolism, Elife 8 (2019).
[16] L. Qin, W. Liu, H. Cao, G. Xiao, Molecular mechanosensors in osteocytes, Bone Res. 8 (2020) 23.
[17] C. Zhang, H.W. van Essen, D. Sie, D. Micha, G. Pals, J. Klein-Nulend, N. Bravenboer, Mapping the response of human osteocytes in native matrix to mechanical loading using RNA sequencing, JBMR Plus 7 (4) (2023) e10721.
[18] M. Wang, H. Idei, C. Wang, Y. Liang, Y. Liu, Y. Matsuda, K. Takahashi, H. Kamioka, K. Naruse, Effect of mechanical stretching stimulation on maturation of human iPS cell-derived cardiomyocytes co-cultured with human gingival fibroblasts, Sci. Rep. 15 (1) (2025) 30648.
[19] X.J. Li, A.V. Valadez, P. Zuo, Z. Nie, Microfluidic 3D cell culture: potential application for tissue-based bioassays, Bioanalysis 4 (12) (2012) 1509–1525.
[20] M. Farahat, E.S. Hara, R. Anada, G.A.S. Kazi, N.M. Akhter, T. Matsumoto, Mechanotransductive mechanisms of biomimetic hydrogel cues modulating Meckel's cartilage degeneration, Adv. Biol. (Weinh.) 6 (6) (2022) e2101315.
[21] K. Svennersten, M. Berggren, A. Richter-Dahlfors, E.W.H. Jager, Mechanical stimulation of epithelial cells using polypyrrole microactuators, Lab Chip 11 (19) (2011) 3287–3293.
[22] D.H. Cho, S. Aguayo, A.X. Cartagena-Rivera, Atomic force microscopy-mediated mechanobiological profiling of complex human tissues, Biomaterials 303 (2023) 122389.
[23] K. Zhang, C.L. Reeves, M. Moghaddar, K.E. Fox, A. Elbourne, A. Gelmi, At the pointy end of mechanobiology: AFM for transient biomechanical analysis, Adv. Healthc. Mater. 14 (31) (2025) e02026.
[24] K.W. Zhang, C.L. Reeves, J.D. Berry, K.E. Fox, A. Elbourne, A. Gelmi, Live quantitative characterization for stem cell biomechanics, Adv. Mater. Interfaces 12 (22) (2025).
[25] E.E. Charrier, P.A. Janmey, Mechanical properties of intermediate filament proteins, Methods Enzymol. 568 (2016) 35–57.
[26] D. Melling, S. Wilson, E.W.H. Jager, The effect of film thickness on polypyrrole actuation assessed using novel non-contact strain measurements, Smart Mater. Struct. 22 (10) (2013).
[27] A.B. Ortega-Santos, S. Hayano, E.S. Hara, J.G. Martínez, H. Kamioka, E.W.H. Jager, PPy-coated wire actuators for the micromechanostimulation of cells: fabrication and characterization, Small Sci. 6 (3) (2026) e202500639.
[28] J.T. Lu, C.J. Lee, S.F. Bent, H.A. Fishman, E.E. Sabelman, Thin collagen film scaffolds for retinal epithelial cell culture, Biomaterials 28 (8) (2007) 1486–1494.
[29] C.N. Grover, J.H. Gwynne, N. Pugh, S. Hamaia, R.W. Farndale, S.M. Best, R. E. Cameron, Crosslinking and composition influence the surface properties, mechanical stiffness and cell reactivity of collagen-based films, Acta Biomater. 8 (8) (2012) 3080–3090.
[30] Z.-Y. Qiu, Y. Cui, X.-M. Wang, Chapter 1 - natural bone tissue and its biomimetic, in: X.-M. Wang, Z.-Y. Qiu, H. Cui (Eds.), Mineralized Collagen Bone Graft Substitutes, Woodhead Publishing, 2019, pp. 1–22.
[31] J. Domke, S. Dannohl, W.J. Parak, O. Muller, W.K. Aicher, M. Radmacher, Substrate dependent differences in morphology and elasticity of living osteoblasts investigated by atomic force microscopy, Colloids Surf. B Biointerfaces 19 (4) (2000) 367–379.
[32] T. Bongiorno, J. Kazlow, R. Mezencev, S. Griffiths, R. Olivares-Navarrete, J. F. McDonald, Z. Schwartz, B.D. Boyan, T.C. McDevitt, T. Sulchek, Mechanical stiffness as an improved single-cell indicator of osteoblastic human mesenchymal stem cell differentiation, J. Biomech. 47 (9) (2014) 2197–2204.
[33] H.C. Wells, K.H. Sizeland, H.R. Kayed, N. Kirby, A. Hawley, S.T. Mudie, R. G. Haverkamp, Poisson's ratio of collagen fibrils measured by small angle X-ray scattering of strained bovine pericardium, J. Appl. Phys. 117 (4) (2015).
[34] Y. Weng, Z. Wang, H. Sitosari, M. Ono, H. Okamura, T. Oohashi, O-GlcNAcylation regulates osteoblast differentiation through the morphological changes in mitochondria, cytoskeleton, and endoplasmic reticulum, Biofactors 51 (1) (2025) e2131.
[35] J. Dockes, K.M. Oudyk, M. Torabi, A.I. de la Vega, J.B. Poline, Mining the neuroimaging literature, Elife 13 (2025).
[36] E. Smela, Microfabrication of PPy microactuators and other conjugated polymer devices, J. Micromech. Microeng. 9 (1) (1999) 1–18.
[37] D. Melling, J.G. Martinez, E.W.H. Jager, Conjugated polymer actuators and devices: progress and opportunities, Adv. Mater. 31 (22) (2019).
[38] X. Zhou, S. Zhu, J. Li, A. Mateus, C. Williams, J. Gilthorpe, L.J. Backman, Mechanical loading modulates AMPK and mTOR signaling in muscle cells, J. Proteome Res. 23 (10) (2024) 4286–4295.
[39] D.P. Nicolella, D.E. Moravits, A.M. Gale, L.F. Bonewald, J. Lankford, Osteocyte lacunae tissue strain in cortical bone, J. Biomech. 39 (9) (2006) 1735–1743.
[40] M. Hammerman, P. Blomgran, A. Dansac, P. Eliasson, P. Aspenberg, Different gene response to mechanical loading during early and late phases of rat Achilles tendon healing, J. Appl. Physiol. (1985) 123 (4) (2017) 800–815.
[41] A. Kawata, Y. Mikuni-Takagaki, Mechanotransduction in stretched osteocytes–temporal expression of immediate early and other genes, Biochem. Biophys. Res. Commun. 246 (2) (1998) 404–408.
[42] S.M. Tanaka, H.B. Sun, R.K. Roeder, D.B. Burr, C.H. Turner, H. Yokota, Osteoblast responses one hour after load-induced fluid flow in a three-dimensional porous matrix, Calcif. Tissue Int. 76 (4) (2005) 261–271.
[43] J.H. Koo, S.W. Plouffe, Z. Meng, D.H. Lee, D. Yang, D.S. Lim, C.Y. Wang, K.L. Guan, Induction of AP-1 by YAP/TAZ contributes to cell proliferation and organ growth, Genes Dev. 34 (1–2) (2020) 72–86.
[44] R. Gozzelino, V. Jeney, M.P. Soares, Mechanisms of cell protection by heme oxygenase-1, Annu. Rev. Pharmacol. Toxicol. 50 (2010) 323–354.
[45] T. Takahashi, H. Shimizu, H. Morimatsu, K. Maeshima, K. Inoue, R. Akagi, M. Matsumi, H. Katayama, K. Morita, Heme oxygenase-1 is an essential cytoprotective component in oxidative tissue injury induced by hemorrhagic shock, J. Clin. Biochem. Nutr. 44 (1) (2009) 28–40.
[46] J.M. Salvador, J.D. Brown-Clay, A.J. Fornace Jr., Gadd45 in stress signaling, cell cycle control, and apoptosis, Adv. Exp. Med. Biol. 793 (2013) 1–19.
[47] A. Schafer, Gadd45 proteins: key players of repair-mediated DNA demethylation, Adv. Exp. Med. Biol. 793 (2013) 35–50.
[48] K.S. Min, Y.H. Hwang, H.J. Ju, H.S. Chang, K.H. Kang, S.H. Pi, S.K. Lee, S.K. Lee, E. C. Kim, Heme oxygenase-1 mediates cytoprotection against nitric oxide-induced cytotoxicity via the cGMP pathway in human pulp cells, Oral Surg. Oral Med. Oral Pathol. Oral Radiol. Endod. 102 (6) (2006) 803–808.